INTERPRETATION OF AEROSOL MASS SCATTERING EFFICIENCY OVER NORTH AMERICA USING GROUND BASED MEASUREMENTS FROM THE IMPROVE NETWORK

by

Robyn Latimer

Submitted in partial fulfillment of the requirements
for the degree of Master of Science

at

Dalhousie University
Halifax, Nova Scotia
February 2018

Table of Contents

List of Tables

List of Figures

Abstract

Aerosol mass scattering efficiency affects climate forcing calculations, atmospheric visibility, and the interpretation of satellite observations of aerosol optical depth. We evaluated the representation of aerosol mass scattering efficiency (α_{sp}) in the GEOS-Chem chemical transport model over North America using collocated measurements of aerosol scatter and mass from IMPROVE network sites between 2000-2015. We found a positive bias in mass scattering efficiency given current assumptions of aerosol size distributions and particle hygroscopicity in the model. We found that overestimation of mass scattering efficiency was most significant in dry (RH<35%) and midrange humidity (35%<RH<65%) conditions, with biases of 87% and 38%, respectively. To address these biases, we investigated assumptions surrounding the two largest contributors to fine aerosol mass, organic and secondary inorganic aerosols. Inhibiting hygroscopic growth of SIA below 35% RH and decreasing the dry geometric mean radius (r_g), from 0.069 μm for SIA and 0.073 μm for OA to 0.058 μm for both aerosol types, significantly decreased the bias observed in dry conditions from 87% to 13%. Implementation of a widely used alternative representation of hygroscopic growth following κ-Kohler theory for secondary inorganic (κ=0.58) and organic aerosols (κ=0.10) eliminated the overall bias in α_{sp}. Simulated average α_{sp} over North America increased by 12%, with larger increases of 20-40% in Northern regions with high RH and hygroscopic aerosol fractions, and decreases in α_{sp} up to 15% in southwestern U.S. where dust fractions are high and RH is low.

List of Abbreviations and Symbols Used

AERONET	Aerosol Robotics Network
AOD	Aerosol Optical Depth
BC	Black Carbon
CCN	Cloud Condensation Nuclei
EC	Elemental Carbon
ERH	Efflorescence Relative Humidity
GADS	Global Aerosol Data Set
GEOS	Goddard Earth Observing System
GF	Growth Factor
GMAO	Global Modeling Assimilation Office
ICARTT	International Consortium for Atmospheric Research on Transport and Transformation
IMPROVE	Interagency Monitoring of Protected Visual Environments
MERRA-2	Modern-Era Retrospective analysis for Research and Applications, Version 2
NASA	National Aeronautics and Space Administration
OA	Organic Aerosol
OC	Organic Carbon
OM	Organic Matter
PSD	Particle Size Distribution
$PM_{2.5}$	fine particulate matter with diameter less than 2.5 μm
PM_{10}	particulate matter with diameter less than 10 μm
PM_{coarse}	particulate matter with diameter between 2.5 and 10 μm
RH	Relative humidity
SIA	Secondary Inorganic Aerosol
SPARTAN	Surface Particulate Matter Network
α_{ext}	mass extinction efficiency
$\alpha_{GC,j}$	GEOS-Chem species specific mass scattering efficiency
α_{sp}	mass scattering efficiency
a_w	water activity

b_{sp}	particle light scatter
D	total particle diameter
D_d	dry particle diameter
$Dust_{PM2.5}$	dust with diameter smaller than 2.5 μm
$Dust_{PMc}$	dust with diameter between 2.5 and 10 μm
κ	volume hygroscopicity parameter
κ_s	volume hygroscopicity parameter for secondary inorganic aerosol
κ_o	volume hygroscopicity parameter for organic aerosol
M	mass concentration
σ	geometric standard deviation
ρ	dry mass density
Q_w	ambient extinction efficiency
R_d	dry effective radius
r_g	geometric mean radius
R_w	ambient effective radius
SSA_w	ambient single scattering albedo
V_d	dry particulate matter volume
V_w	water volume

Acknowledgements

I would like to thank my supervisor, Dr. Randall Martin, for his guidance and support during my time at Dalhousie. This project would not have been possible without his valuable insight and ideas. I would also like to thank my committee members, Dr. Rachel Chang and Dr. Glen Lesins, for their input on this project.

I would like to thank all past and current members of the Atmospheric Composition Analysis Group who have assisted me during this time. I would especially like to thank Crystal Weagle, whose guidance and willingness to help was always appreciated.

I am grateful to the IMPROVE and AERONET teams for making available the data used in this study. I would also like to acknowledge Environment and Climate Change Canada, for supplying nephelometer data at the site in Egbert, Ontario.

Finally, I would like to thank my family and friends. This would not have been possible without their love and support.

Chapter 1. Introduction

The interaction of atmospheric aerosols with radiation has substantial implications for the direct radiative effects of atmospheric aerosols, atmospheric visibility, and satellite retrievals of aerosol optical properties. The direct radiative effects of aerosols remain a major source of uncertainty in total anthropogenic effective radiative forcing (Myhre et al., 2013). Atmospheric visibility affects the appearance of landscape features, which is of particular concern in national parks and wilderness areas (Malm et al., 1994)**.** Gaining insight into the concentration and composition of atmospheric aerosols via interpretation of satellite retrievals of aerosol optical depth (AOD) also relies heavily on an understanding of the interaction of aerosols with radiation (Kahn et al., 2005). Analysis of collocated measurements of aerosol scatter, mass, and composition could offer valuable insight into aerosol optical properties.

Current chemical transport models and global circulation models often calculate atmospheric extinction due to aerosols from speciated aerosol mass concentrations using a composition and size dependent mass extinction efficiency (α_{ext}, $m^2\ g^{-1}$). Many of these models use aerosol optical and physical properties defined by the Global Aerosol Data Set (GADS), based on measurements performed between 1970-1995 (Koepke et al., 1997). The subsequent growth in long term aerosol monitoring offers an exciting possibility to further improve model representation of aerosol physical and optical properties. The Interagency Monitoring of Protected Visual Environments (IMPROVE) network offers long-term collocated measurements since 1987 of particle scatter (b_{sp}),

relative humidity (RH), fine particulate mass concentrations less than 10 μm (PM_{10}) and less than 2.5 μm ($PM_{2.5}$) mass as well as chemical composition at sites across the United States and Canada (Malm et al., 1994; Malm et al., 2004). These collocated measurements provide direct measurements of mass scattering efficiency (α_{sp}) across North America to evaluate and improve the mass scattering efficiency currently used in models.

Several prior studies have analyzed mass scattering efficiencies. Hand et al. (2007) performed an extensive review that examined and compared mass scattering efficiencies calculated from ground based measurements from approximately 60 mostly short-term studies. The study by Malm & Hand (2007) applied IMPROVE network data between 1987-2003 to evaluate mass scattering efficiency of organic and inorganic aerosols at 21 IMPROVE sites. Our study builds upon these previous studies by reducing initial assumptions regarding size and hygroscopicity of inorganic and organic aerosols and by using measurements of particle speciation, mass and scatter to inform the representation of these properties. We interpret long term measurement data to obtain a representation of mass scattering efficiency that can be used across an array of conditions and locations to facilitate incorporation into chemical transport models.

Here we interpret collocated measurements of $PM_{2.5}$, PM_{10}, b_{sp} and relative humidity (RH) from the IMPROVE network to understand factors affecting the representation of mass scattering efficiency. Section 2 provides a description of IMPROVE network measurements, of the GEOS-Chem chemical transport model, and of an alternate aerosol hygroscopic growth scheme. Descriptions of particle scatter and mass scattering

efficiency calculations in GEOS-Chem, and the incorporation of IMPROVE network measurements into these calculations are described in Section 3. In Section 4, we present an analysis of the current representation of mass scattering efficiency, and identify changes that improve the consistency with observations. The impact of these changes on GEOS-Chem simulated mass scattering efficiency, as well as on agreement between the GEOS-Chem model and observations from the IMPROVE network are described in section 5.

Chapter 2. Methods

2.1 IMPROVE Network Measurements

The IMPROVE network (Malm et al., 1994) is a long-term monitoring program established in 1987 to monitor visibility trends in national parks and wilderness areas in the United States. The network offers collocated measurements of $PM_{2.5}$ speciation, $PM_{2.5}$ and PM_{10} gravimetric mass, b_{sp} and RH that we interpret to understand mass scattering efficiency.

The IMPROVE particle sampler collects $PM_{2.5}$ and PM_{10} on filters. Sampling occurs over a 24h period every third day. Collected $PM_{2.5}$ is analyzed for fine gravimetric mass, elemental concentrations (including Al, Si, Ca, Fe, Ti), ions (SO_4^{2-}, NO_3-, NO_2^-, Cl^-), and organic and elemental carbon. Collected PM_{10} undergoes gravimetric analysis for coarse mass (Malm et al., 1994).

The particle scattering coefficient (b_{sp}) is measured at 550 nm at a subset of IMPROVE sites using OPTEC NGN-2 open air integrating nephelometers (Malm et al., 2007). b_{sp} is measured hourly at ambient air temperature and relative humidity; all three parameters are recorded. We filter b_{sp} data to exclude measurements likely affected by meteorological interference such as fog. These conditions include an RH threshold of 95%, a maximum b_{sp} threshold of 5000 Mm^{-1} and an hourly rate of change threshold for b_{sp} of 50 Mm^{-1}, following IMPROVE filtering protocol (IMPROVE, 2004).

For this study, we select sites where fine aerosol mass and speciation measurements are collocated with IMPROVE nephelometers between 2000-2015. We exclude coastal sites between 2000-2005, since reliable estimates of sea salt concentrations were unavailable prior to 2005, and since sea salt can contribute significantly to b_{sp} in coastal conditions of high RH due to its highly hygroscopic nature (Lowenthal & Kumar, 2006). We use only days with coincident mass and scatter measurements. Additionally, only days with a minimum of 23 hourly measurements are used, to reduce influence of meteorological interference.

Figure 1 shows at the 30 sites used in this study the average b_{sp}, PM_{10} and $PM_{2.5}$ measured between 2000-2015. Measured b_{sp} values vary by a factor of 7 with scatter below 20 Mm^{-1} across the southwest U.S., and scatter above 50 Mm^{-1} across the southeast U.S. Measured PM_{10} concentrations vary by a factor of 3 with values below 6 $\mu g\ m^{-3}$ in the west to above 14 $\mu g\ m^{-3}$ in the southeast. Measured $PM_{2.5}$ concentrations also vary by a factor of 3, with values below 3 $\mu g\ m^{-3}$ in the west to above 9 $\mu g\ m^{-3}$ in the southeast.

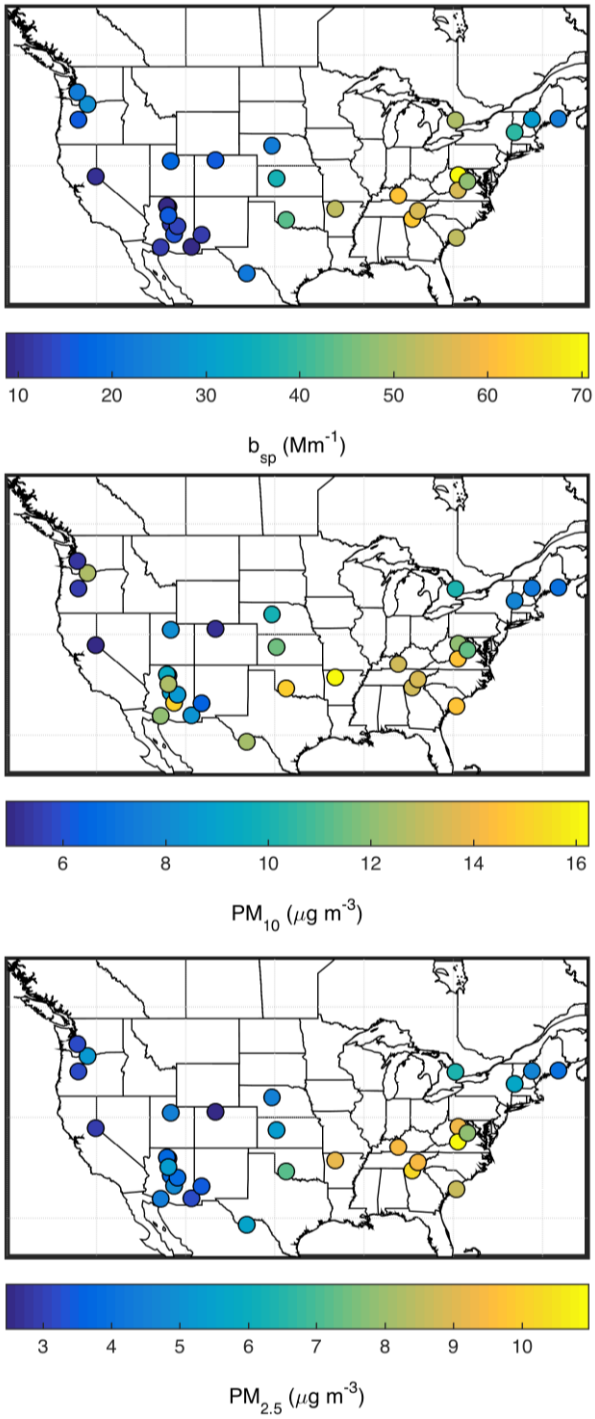

Figure 1. Map of IMPROVE sites with collocated scatter (bsp), PM_{10} and $PM_{2.5}$ measurements in North America between 2000-2015. Overlaying circles represent average collocated bsp (top), PM_{10} (middle) and $PM_{2.5}$ (bottom).

2.2 GEOS-Chem Simulation

We simulate hourly $PM_{2.5}$ and PM_{10} mass concentrations and particle scatter using version 11.01 of the global chemical transport model GEOS-Chem (http://geos-chem.org). The GEOS-Chem model is driven by assimilated meteorology from the Goddard Earth Observation System (GEOS MERRA-2) of the NASA Global Modeling and Assimilation Office (GMAO). Our simulation is conducted at 2° x 2.5° resolution over 47 vertical levels.

GEOS-Chem simulates detailed aerosol-oxidant chemistry (Bey et al., 2001; Park et al., 2004). The aerosol simulation includes the sulfate-nitrate-ammonium system (Park et al., 2004), primary (Park et al., 2003; Wang et al., 2014) and secondary (Pye et al., 2010) carbonaceous aerosols, mineral dust (Fairlie et al., 2007) and sea salt (Jaeglé et al., 2011). Organic matter (OM) is estimated from primary organic carbon (OC) using spatially and seasonally varying OM/OC ratios at 0.1° x 0.1° resolution (Philip et al., 2014). The thermodynamic equilibrium model ISORROPIA-II (Fountoukis & Nenes, 2007), implemented by Pye et al. (2009), is used to calculate gas-aerosol partitioning. Aerosol physical and optical properties are defined by the Global Aerosol Data Set (GADS) (Koepke et al., 1997), as implemented by Martin et al. (2003), with modifications to dry size distributions (Drury et al., 2010) and dust mass partitioning (Ridley et al., 2012). Total $PM_{2.5}$ is calculated following van Donkelaar et al. (2010), but at 40% RH here for consistency with the IMPROVE network gravimetric analysis in the range of 30-50% RH

(Solomon et al., 2014). Particle scatter and aerosol optical depth are calculated at ambient RH based on dry species mass concentrations and aerosol physical and optical properties.

We conduct a 1 year simulation for the year 2006, to represent the period of greatest measurement density of collocated b_{sp} and PM sites over North America. We archive model fields every hour over North America. We simulate $PM_{10,}$ $PM_{2.5}$ and b_{sp}, allowing for the comparison of model mass scattering efficiency to that measured at IMPROVE network sites over North America.

2.3 Calculating mass scattering efficiency (α_{sp})

One method of calculating mass scattering efficiencies from measurements involves b_{sp} measurements and particle mass concentration measurements (M_{meas}). Mass scattering efficiency of a given aerosol population can be defined as the ratio of particle scatter to mass.

$$\alpha_{sp,meas} = \frac{b_{sp,meas}}{M_{meas}} \quad (1)$$

Hourly mass scattering efficiencies are calculated at IMPROVE sites using measurements of b_{sp} and mass concentrations from the IMPROVE network, treating IMPROVE mass concentrations as constant over each 24h sampling period. Total scatter is typically dominated by fine mode aerosols, but in certain conditions coarse dust can also make a significant contribution (White et al., 1994). Thus, measured PM_{10} mass is used in the denominator of equation 1.

We compare these measured α_{sp} with calculated α_{sp} based on species specific mass scattering efficiencies ($\alpha_{GC,j}$) used in GEOS-Chem, contrained with mass concentrations (M_j) and PM_{10} mass measured by IMPROVE.

$$\alpha_{sp,calc} = \frac{b_{sp,calc}}{PM_{10,meas}} = \frac{\sum_j \alpha_{GC,j} M_j}{PM_{10,meas}} \quad (2)$$

This approach enables isolation of the mass scattering efficiencies used in GEOS-Chem from the species concentrations.

2.3 Introducing an Alternate Hygroscopic Growth Scheme

We examine for GEOS-Chem the use of a widely adopted alternate hygroscopic growth scheme, in which aerosol hygroscopic growth is defined by a single parameter, κ (Petters and Kreidenweis 2007, 2008, 2013). This representation of water uptake by aerosols was originally developed for supersaturated CCN conditions, but in recent years has been used extensively in subsaturated conditions (Dusek et al., 2011; Hersey et al., 2013).

The hygroscopic parameter κ is defined by

$$\frac{1}{a_w} = 1 + \kappa \frac{V_d}{V_w} \quad (3)$$

where V_d is dry particulate matter volume, V_w is the water volume and a_w is water activity (Petters & Kreidenweis, 2013), which can be approximated to the first order as a_w=RH/100. The diameter growth factor ($GF=D/D_d$) can be expressed (Snider et al., 2016) as

$$GF = \left(1 + \kappa \frac{RH}{100-RH}\right)^{1/3} \quad (4)$$

where D is the wet aerosol radius and D_d is the dry aerosol radius. Typically, κ_v is in the range of 0.5-0.7 for SIA (Hersey et al., 2013; Kreidenweis et al., 2008; Petters & Kreidenweis, 2007) and 0-0.2 for OA (Duplissy et al., 2011; Kreidenweis et al., 2008; Rickards et al., 2013; Snider et al., 2016).

Figure 2 shows the diameter growth factor as a function of relative humidity following κ-Kohler theory, as well as GEOS-Chem default hygroscopic growth for SIA and OA. The GEOS-Chem default hygroscopic growth schemes are characterized by larger growth at low RH and smaller growth at high RH for both secondary inorganic and organic aerosols. The RH value at which κ growth exceeds default growth is 91% for OA and 70% for SIA.

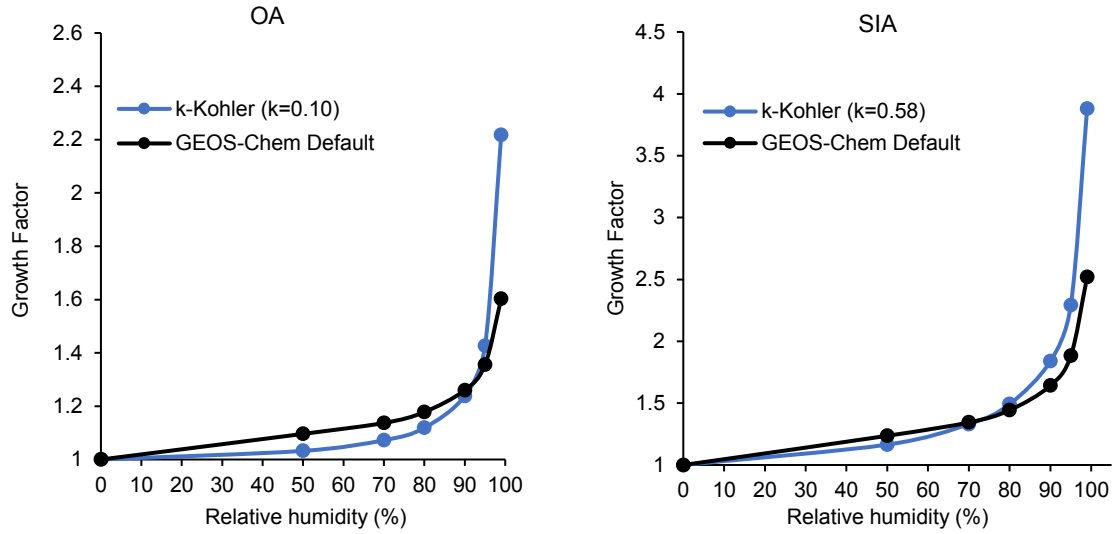

Figure 2. Hygroscopic growth factor curves for OA(left) and SIA (right), with GEOS-Chem default growth in black and k-Kohler growth in blue.

Chapter 3. Background

3.1 b_{sp} and α_{sp} Calculations in GEOS-Chem

In GEOS-Chem, surface level b_{sp} is calculated using model particle mass concentrations and local relative humidity, as well as predefined mass densities and aerosol optical properties for each aerosol component following:

$$b_{sp} = \sum_{species,i} \frac{\frac{3}{4} * \left(\frac{R_{w,i}}{R_{d,i}}\right)^2 * M_{d,i} * Q_{w,i} * SSA_{w,i}}{\rho_{d,i} * R_{d,i}} \quad (5)$$

where ρ_d is the dry particle mass density, R_w is the effective radius (defined as the ratio of the third to second moment of an aerosol size distribution), R_d is the dry effective radius, M_d is the dry surface level mass concentration, Q_w is the extinction efficiency, and SSA_w

is the single scattering albedo. Parameters with the subscript w indicate values at ambient RH. Species included in this calculation are SO_4^{2-}, NH_4^+, NO_3^-, BC, OM and fine and coarse dust and sea salt.

Dividing equation (5) by total surface level PM_{10} results in the following equation for mass scattering efficiency

$$\alpha_{sp} = \frac{B_{sp}}{PM_{10}} = \sum_{species,i} \frac{\frac{3}{4} * \left(\frac{R_{w,i}}{R_{d,i}}\right)^2 * \frac{M_{d,i}}{PM_{10}} * Q_{w,i} * SSA_{w,i}}{\rho_{d,i} * R_{d,i}} \quad (6)$$

The effective radius, extinction efficiency and single scattering albedo in equation 5 and 6 are obtained from GEOS-Chem optical tables for the ambient RH values measured by IMPROVE. Dry mass density ρ_d is specified for each aerosol species in GEOS-Chem (Table 1). $M_{d,i}$ and PM_{10} are obtained from IMPROVE network measurements of aerosol mass and composition. α_{sp} calculated by equation (6) is compared to α_{sp} directly measured by the IMPROVE network.

Component	r_g (μm)	σ	ρ_d (g/cm^3)
Sulfate/Nitrate/Ammonium	0.070	1.6	1.7
Organic Carbon	0.073	1.6	1.3
Black Carbon	0.020	1.6	1.8
SeaSalt (fine)	0.085	1.5	2.2
SeaSalt (coarse)	0.401	1.8	2.2
Brown Carbon	0.073	1.6	1.3
Dust 1 a-d	0.030-0.170	2.2	2.5
Dust 2	0.265	2.2	2.65
Dust 3	0.530	2.2	2.65
Dust 4	0.845	2.2	2.65

Table 1. Current microphysical properties of each aerosol species in GEOS-Chem. r_g represents the dry geometric mean radius (μm) and σ the geometric standard deviation of the lognormal size distributions assumed for each species. ρ_d represents the dry mass densities of each species (g/cm^3).

Mass scattering efficiency is dependent on particle density, refractive index and particle size. Mass scattering efficiency is typically most dependent on aerosol size, which is dictated by both the dry size distribution chosen to represent a given aerosol species, and by the hygroscopic growth scheme used to represent aerosol water uptake for hydrophilic species.

3.2 Incorporating IMPROVE Network Measurements

The IMPROVE network measures $PM_{2.5}$ mass and speciation and PM_{10} mass every three days. The IMPROVE particle sampler consists of four independent modules with separate inlets and pumps. The first three modules (A, B and C) collect only fine particulate matter ($PM_{2.5}$), while the 4th module (D) collects both fine and coarse particles (PM_{10}). Module A collects $PM_{2.5}$ on a Teflon filter, which undergoes gravimetric analysis

for total $PM_{2.5}$ mass and x-ray florescence for elemental concentrations (including Al, Si, Ca, Fe, Ti). The nylon filter in module B undergoes ion chromatography analysis for SO_4^{2-}, NO_3^-, NO_2^- and Cl^-. Module C contains a quartz filter that is analyzed for organic and elemental carbon via thermal optical reflectance. The Teflon filter in module D undergoes gravimetric analysis for PM_{10} mass (Malm et al., 1994; Malm et al., 2004). Prior to gravimetric analysis, filters A and D undergo equilibration at 30-50% RH and 20-25 °C for several minutes (Solomon et al., 2014).

To calculate mass scattering efficiency via equation (6), we require mass concentration data for SO_4^{2-}, NO_3^-, NH_4^+, BC, OM and fine and coarse dust and sea salt. Nitrate is measured directly via ion chromatography, sulfate is calculated under the assumption that all elemental S is from sulfate (equation 7).

$$SO_4^{2-}=4.125*[S] \quad (7)$$

Ammonium is not directly measured, but it is assumed by the IMPROVE network that SO_4^{2-} and NO_3^- are fully neutralized by NH_4^+ to form $(NH_4)_2SO_4$ and NH_4NO_3. Under this assumption, ammonium concentrations are calculated via

$$NH4^+= 0.2254* [NH_4NO_3] + 0.2730*[(NH_4)_2SO_4] \quad (8)$$

Following IMPROVE protocol, the remaining aerosol species mass concentrations are calculated as follows

$$\text{Fine dust} = 2.2*[Al]+2.49*[Si]+1.63*[Ca]+2.42*[Fe]+1.94*[Ti] \quad (9)$$

$$\text{Organic Mass by Carbon} = 1.8*[OC] \quad (10)$$

$$\text{Elemental Carbon} = [EC] \quad (11)$$

$$\text{Sea Salt} = 1.8 * [Cl^-] \quad (12)$$

The factor of 1.8 in equation 12 corresponds to the OM/OC ratio assumed by the IMPROVE network (Malm & Hand, 2007). IMPROVE defines the sea salt concentration as the concentration of the chloride ion, $[Cl^-]$, multiplied by 1.8 (Malm et al., 2007).

The GEOS-Chem model partitions OM into hydrophilic and hydrophobic fractions, so the same is done for OM measured by IMPROVE. OM in remote regions tends to be highly oxidized, and oxidation level of organics has been shown to positively correlate with hygroscopicity (Duplissy et al., 2011; Jimenez et al., 2009; Ng et al., 2010). We treat measured OM as 90% hydrophilic, due to the rural nature of IMPROVE sites. EC is treated as 50% hydrophilic. As speciation of coarse material is unavailable, we treat all coarse material as crustal in origin, an assumption that may breakdown at coastal sites.

Dust aerosols are partitioned into four size bins in the GEOS-Chem model. Mineral dust aerosols in each of these bins are defined by different microphysical and optical properties. These dust bins are partitioned into fine and coarse dust following Fairlie et al. (2007, 2010)

$$\text{Dust}_{PM2.5} = \text{Bin1} + 0.38\ \text{Bin2} \quad (13)$$

$$\text{Dust}_{PMc} = 0.62\ \text{Bin2} + \text{Bin3} + \text{Bin4} \quad (14)$$

We partition fine and coarse dust measured by the IMPROVE network into these four bins. We do so using the dust particle size distribution (PSD) described by Zhang et al. (2013). The size resolved mass fractions of total dust into each of the GEOS-Chem dust size bins using this distribution are shown in table 2. We derive the following equations for partitioning of IMPROVE measured dust into GEOS-Chem size bins using this PSD and equations (13) and (14).

$$\text{Bin 1 (0.2-2.0 } \mu\text{m)} = 0.513 * \text{Dust}_{PM2.5} \quad (15)$$

$$\text{Bin 2 (2.0-3.6 } \mu\text{m)} = 0.487 * \text{Dust}_{PM2.5} + 0.148 * \text{Dust}_{PMc} \quad (16)$$

$$\text{Bin 3 (3.6-6.0 } \mu\text{m)} = 0.410 * \text{Dust}_{PMc} \quad (17)$$

$$\text{Bin 4 (6.0-12.0 } \mu\text{m)} = 0.449 * \text{Dust}_{PMc} \quad (18)$$

Radii (μm)	**Bin 1 (0.1-1.0)**	**Bin 2 (1.0-1.8)**	**Bin 3 (1.8-3.0)**	**Bin 4 (3.0-6.0)**
IMP_PSD	7.7 %	19.2 %	34.9 %	38.2 %

Table 2. Size resolved mass fractions of total dust into each of the GEOS-Chem dust size bins.

Chapter 4. Results

4.1 Understanding the Current Representation of α_{sp}

Figure 3 shows measured vs. calculated mass scattering efficiency using GEOS-Chem default optical tables. Each point represents the average α_{sp} at an IMPROVE site. A significant correlation (r=0.96) is apparent, however a bias in α_{sp} is evident from the offset. A positive correlation between average mass scattering efficiency and RH is apparent; sites with low average RH have low average α_{sp} and vice versa.

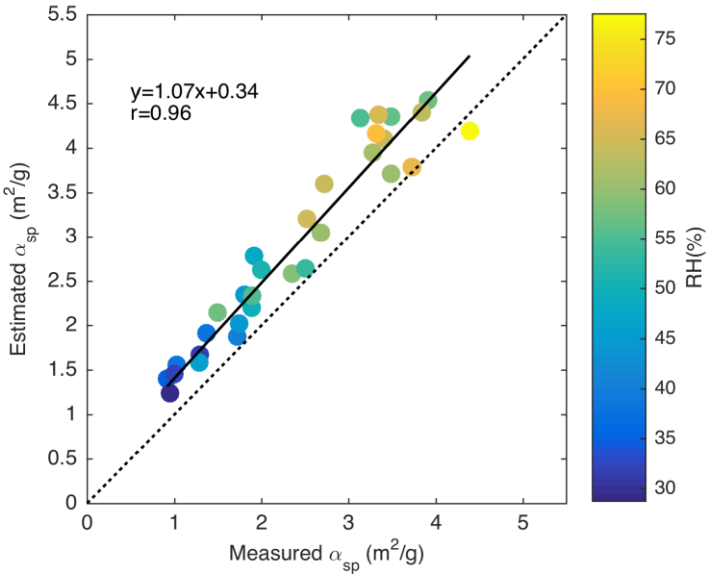

Figure 3. Average measured vs estimated α_{sp} at IMPROVE sites using GEOS-Chem default optical tables. The 1:1 line is black. Slope, offset and correlation coefficient are inset.

To further investigate the possible RH dependence of this bias, we separate our analysis of α_{sp} into 3 relative humidity groupings: 0-35% (low), 35-65% (mid) and 65-95% (high). The blue dots in Figure 4 show estimated vs measured α_{sp} for each RH range. In the low RH case, a significant overestimation of mass scattering efficiency is apparent at

most sites, with a bias of 87%. In the mid RH case, overestimation of α_{sp} is less significant but still apparent with a bias of 38%. At high RH, overestimation is least significant.

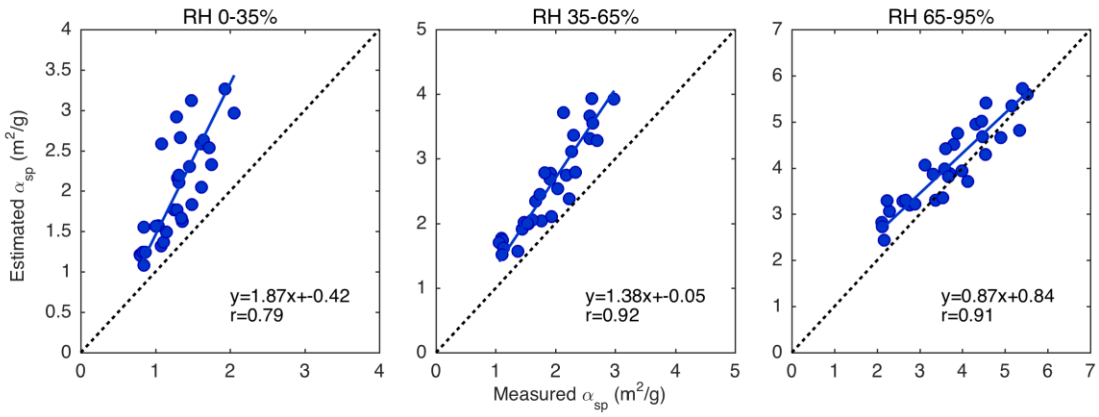

Figure 4. Average measured versus estimated α_{sp} at IMPROVE sites using GEOS-Chem default optical tables for measurements taken in 0-35% RH (left), 35-65% RH (center) and 65-95% RH (right) conditions. The 1:1 line is black. Slope, offset and correlation coefficient are inset.

To further understand the source of the bias in estimated mass scattering efficiency, we now examine estimated α_{sp} in conditions dominated by different aerosol types. Figure 5 shows measured vs estimated α_{sp} for conditions where $PM_{2.5}$ is dominated (>60%) by secondary inorganic aerosol, organic aerosol and dust, as well conditions where PM_{10} is dominated (>60%) by PM_{coarse} (PM_{10}-$PM_{2.5}$). The scatterplot in the SIA dominant case resembles the overall relationship shown in Figure 3. α_{sp} is overestimated at most sites, with significant correlation (r=0.89) and a bias evident in the offset of 0.72. Where OA is the dominant component of $PM_{2.5}$, α_{sp} is largely overestimated. In this case, α_{sp} is accurately estimated at the few sites where average relative humidity is greater than 60%. Where dust is the dominant fine aerosol, correlation is significant (r=0.89) and mass scattering efficiency is accurately estimated at the vast majority of sites, despite a

prominent outlier at a site in the Columbia River Gorge, Washington. The PM_{coarse} dominant case shows significant correlation (r=0.90) and a slight tendency for overestimation of α_{sp}. As this case is not independent from the other cases, this overestimation is likely linked to the overestimation in the OA and SIA dominant cases as demonstrated below.

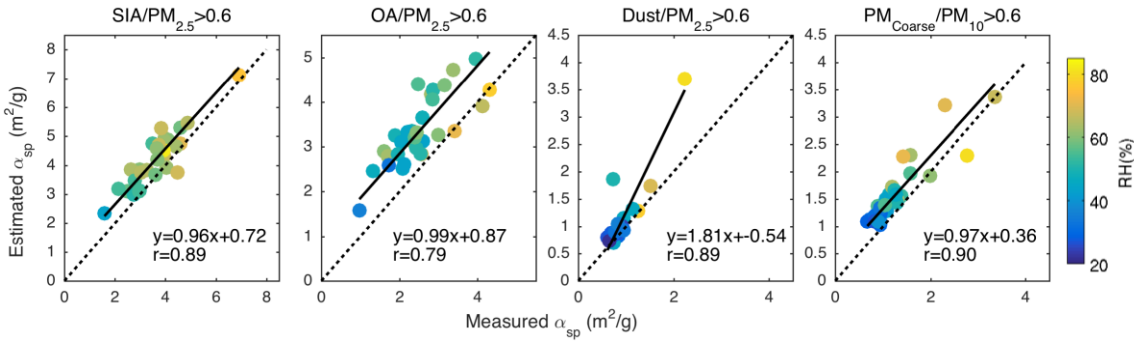

Figure 5. Average measured versus estimated α_{sp} at IMPROVE sites using GEOS-Chem default optical tables using measurements taken in SIA dominant conditions (left), OA dominated conditions, Dust dominant conditions and PM_{coarse} dominated conditions (right). The 1:1 line is black. Slope, offset and correlation coefficient are inset.

These results indicate that the bias in estimated mass scattering efficiency arises mostly due to the representation of the physical and optical properties of secondary inorganic and organic aerosols. The following will focus on improving the representation of physical and optical properties of these two aerosol types.

4.2 Changing the Physical Properties of SIA and OA

Figure 6 shows mass scattering efficiency as a function of aerosol size for secondary inorganic (orange) and organic (blue) aerosols for dry aerosols (solid) and aerosols at 80% RH (dashed lines) as calculated using a Mie algorithm (Mishchenko et al., 1999). The uptake of water decreases aerosol density and decreases the refractive index.

The points in Figure 6 represent the current mass scattering efficiency values of OA and SIA in GEOS-Chem. For both species, α_{sp} does not differ significantly between the RH=0% and RH=80% cases. For dry aerosols, α_{sp}=4.4 m^2/g for OA and α_{sp}=3.2 m^2/g for SIA. In a review of ground-based estimates of aerosol mass scattering efficiencies, Hand et al. (2007) found dry α_{sp} values of 2.5 m^2/g for ammonium sulfate, 2.7 m^2/g for ammonium nitrate, and 3.9 m^2/g for particulate organic matter. These values indicate that the default optical tables in GEOS-Chem currently overestimate mass scattering efficiency of SIA and OA in dry conditions. This reaffirms the overestimation of α_{sp} in dry conditions evident in the left panel of Figure 4. As aerosol size is the strongest determinant of mass scattering efficiency for a given aerosol type, we begin by examining the dry sizes of SIA and OA in GEOS-Chem.

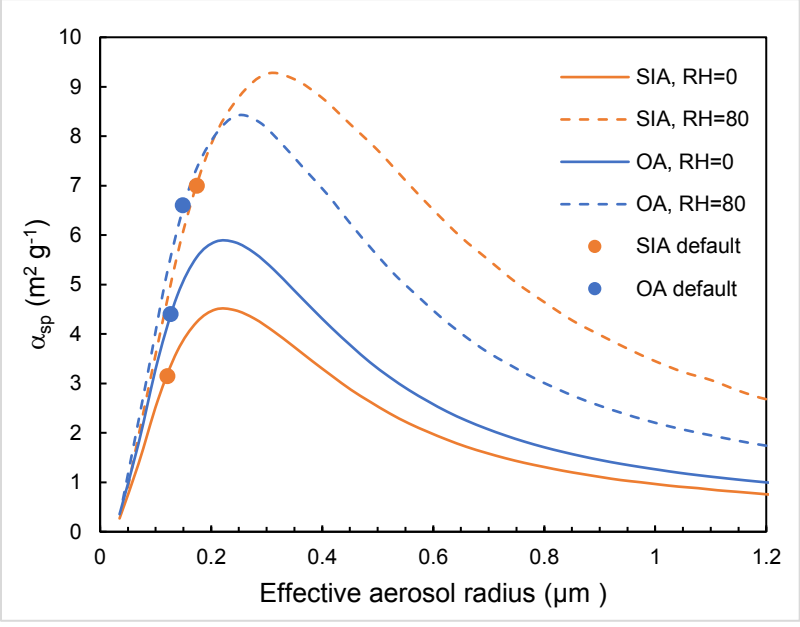

Figure **6**. Mass scattering efficiency (α_{sp}) as a function of aerosol radius for organic aerosol (blue) and secondary inorganic aerosol (orange). Solid lines show α_{sp} for dry aerosol (RH=0%), dashed lines show α_{sp} for acqueous aerosols (RH=80%). Points represent the default size in GEOS-Chem.

The current dry sizes of SIA and OA in GEOS-Chem were informed by measurements from several aircraft campaigns over eastern North America during the summer of 2004 (Drury et al., 2010) as part of the The International Consortium for Atmospheric Research on Transport and Transformation (ICARTT) (Fehsenfeld et al., 2006; Singh et al., 2006). Aerosol surface area and volume distributions fluctuate seasonally in the North Eastern U.S., with summer maximums and winter minimums (Stanier et al., 2004). We divide our analysis at low RH by season, in an effort to discern a seasonal pattern in the overestimation of α_{sp}.

Figure 7 shows seasonal measured vs. estimated mass scattering efficiency in dry conditions. Estimations of α_{sp} are most accurate in the summer, consistent with the dry sizes chosen by Drury et al. (2010) which were informed by summertime size distribution measurements. The overestimation of α_{sp} in all other seasons, most notably in winter, is consistent with the seasonality in aerosol size distributions observed by Stanier et al. (2004).

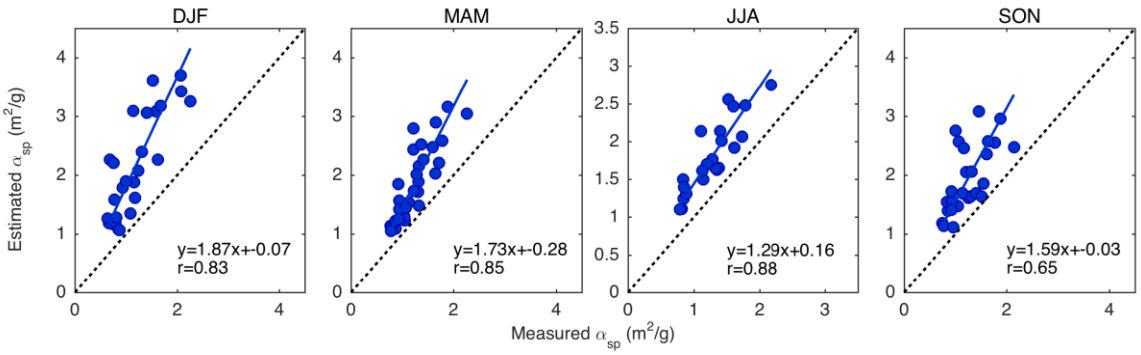

Figure 7. Average measured versus estimated α_{sp} at IMPROVE sites using GEOS-Chem default optical tables for measurements taken in dry conditions (RH<35%) in winter, spring, summer and fall. The 1:1 line is black. Slope, offset and correlation coefficient are inset.

4.2.1 Efflorescence Relative Humidity for SIA

To address the overestimation of mass scattering efficiency in dry conditions illustrated in Figure 4 and 7, we begin by accounting for efflorescence transitions in secondary inorganic aerosols. Efflorescence phase transitions are characterized by nucleation of the crystalline phase followed by rapid evaporation of water. Field measurements have found evidence for these transitions (Martin et al., 2008). The efflorescence relative humidity (ERH) of ammonium sulfate reported in several experimental studies range from 35-40% (Ciobanu et al., 2010). Laboratory tests have shown that mixtures of sulfate-nitrate-ammonium particles will undergo efflorescence when the ammonium sulfate fraction is high (Dougle et al., 1998; Martin et al., 2003). This condition is true at most global measurement sites, with the possible exception of Europe, where particles are nitrate rich (Martin et al., 2003).

We therefore define the hygroscopic growth factor for SIA as 1 for RH ≤ 35%, linearly increasing between 35-40% RH from 1 to $GF_{40\%}$ (calculated by Equation 4), and following the default (or κ-Kohler) growth curve for RH ≥ 40%.

Incorporating an ERH for SIA and consequently inhibiting hygroscopic growth of SIA below 35% RH significantly reduces the overestimation of mass scattering efficiency in dry conditions. In the case of default hygroscopic growth in GEOS-Chem, the overall dry bias in α_{sp} is reduced from 87% to 53%, as shown in Figure 8.

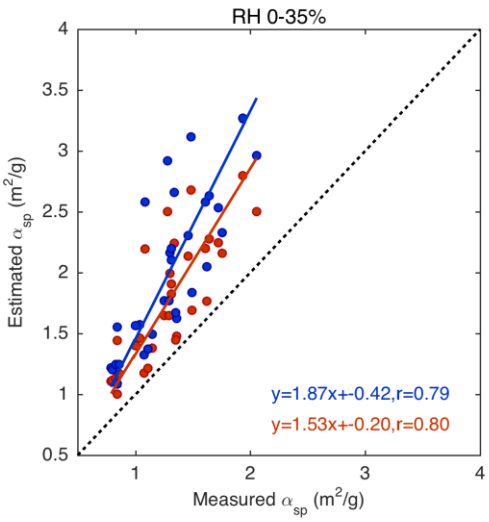

Figure 8. Average measured vs. estimated α_{sp} at IMPROVE sites in dry conditions (RH<35%) using default optical tables (blue) and default optical tables with ERH of 35% (red). The 1:1 line is black. Slope, offset and correlation coefficient are inset.

4.2.2 Aerosol Dry Size

To address the remaining overestimation of mass scattering efficiency in dry conditions we explore different dry sizes of secondary inorganic and organic aerosols. Figure 9 shows the slope of the average measured vs estimated α_{sp} plot for RH<35% for dry radii ranging from 0.050 to 0.074 μm at intervals of 0.001μm, assuming SIA and OA have the same dry size. The slope of the best fit line acts as an indicator of the appropriate dry size for each season. The slope decreases steadily as dry radius is decreased in all seasons. Slope as a function of radius is nearly identical in the spring and fall, diverging slightly for the smallest sizes.

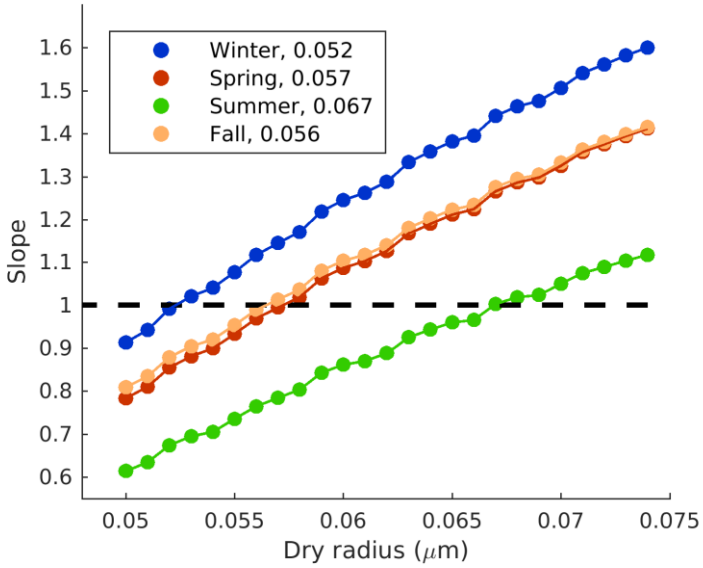

Figure 9. Slope of measured vs. estimated α_{sp} plot versus dry geometric mean aerosol radius, by season. Winter (DJF) is in blue, spring (MAM) in red, summer (JJA) in green and fall (SON) in orange. The line Slope=1 is shown in black. Numbers in the legend represent the dry radius for which slope=1 for each season.

Using the dry radius which gives a slope of unity for each season, we find that dry aerosols are largest in summer (r=0.067 μm), smallest in winter (r=0.052 μm), and in between in spring and fall (0.057 μm and 0.056 μm, respectively). Averaging the sizes from all four seasons results in an annual representative dry radius of 0.058 μm.

Figure 10 shows seasonal measured vs. estimated α_{sp} in dry conditions using this new representative annual geometric mean radius for SIA and OA. This change in geometric mean radius reduces the overestimation of α_{sp} in all seasons, with the largest improvement in spring (slope decreases from 1.73 to 1.01) and winter (slope decreases

from 1.87 to 1.16). Changes in correlation are minor.

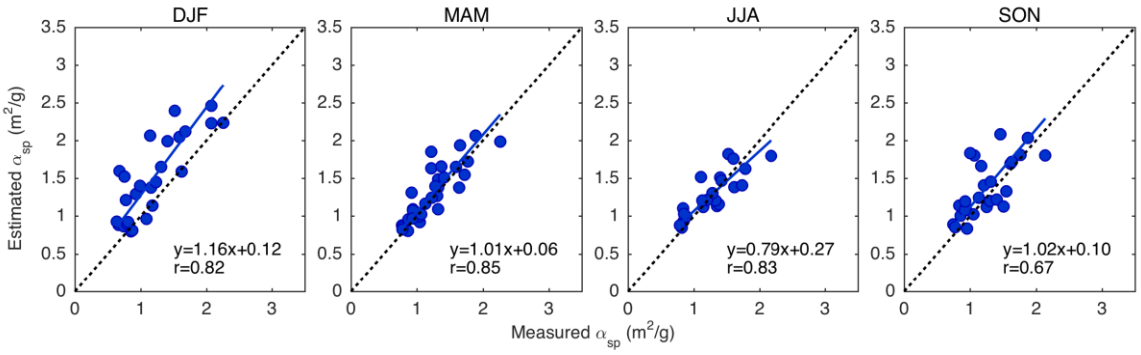

Figure 10. Average measured vs. estimated α_{sp} at IMPROVE sites in dry conditions (RH<35%) using revised optical tables with a geometric mean radius of 0.064 μm for SIA and OA in winter, spring, summer and fall. The 1:1 line is black. Slope, offset and correlation coefficient are inset.

4.2.3 Aerosol Hygroscopicity

We now examine the implementation of the widely adopted κ-Kohler hygroscopic growth scheme described in section 2.3. A range of measured κ values for SIA (κ_s) and OA (κ_o) exist in the literature. We explore the range of possible κ values, using the slope of the measured vs estimated α_{sp} plot as an indicator of the appropriate values.

Figure 11 shows the slope of the measured vs estimated α_{sp} plot for κ_s ranging from 0.5-0.7 and κ_o ranging from 0.08-0.20 in increments of 0.01. Slope increases steadily as κ_s and κ_o increase. We find that slope is equal to one when κ_s =0.58 and a κ_o=0.10. These values are in the middle of the range of measured κ values (Duplissy et al., 2011; Hersey et al., 2013; Kreidenweis et al., 2008; Petters & Kreidenweis, 2007; Rickards et al., 2013).

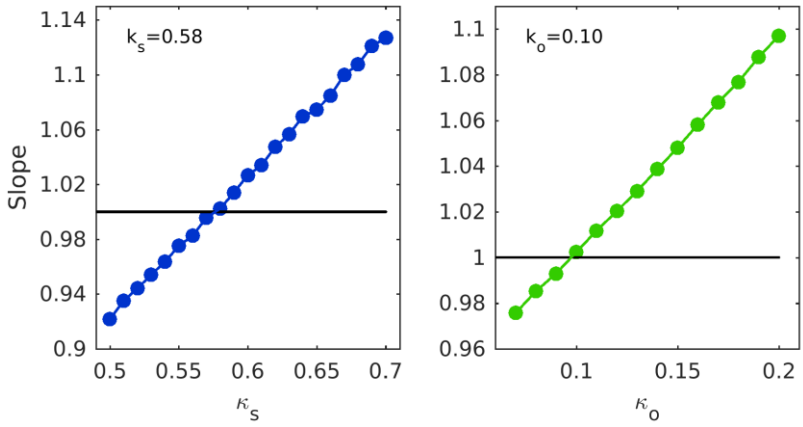

Figure 11. Slope of measured vs. estimated α_{sp} plot as a function of κ_s (left) and κ_o (right). The line slope=1 is shown in black. κ_s and κ_o values for which slope=1 are inset.

Using the revised dry size of 0.058 μm and the κ-Kohler theory of hygroscopic growth, we calculate revised physical and optical properties for SIA and OA over a range of RH values. Table A.1 compares geometric mean radius, effective radius, extinction efficiency and single scattering albedo for the default and revised optical tables at 8 relative humidity values.

Figure 12 shows the measured vs estimated mass scattering efficiency using these revised optical tables for SIA and OA. The overestimation of mass scattering efficiency has been eliminated with these revised aerosol properties, with a slope of 1.00 and an offset of 0.05. Correlation remains significant at r=0.97.

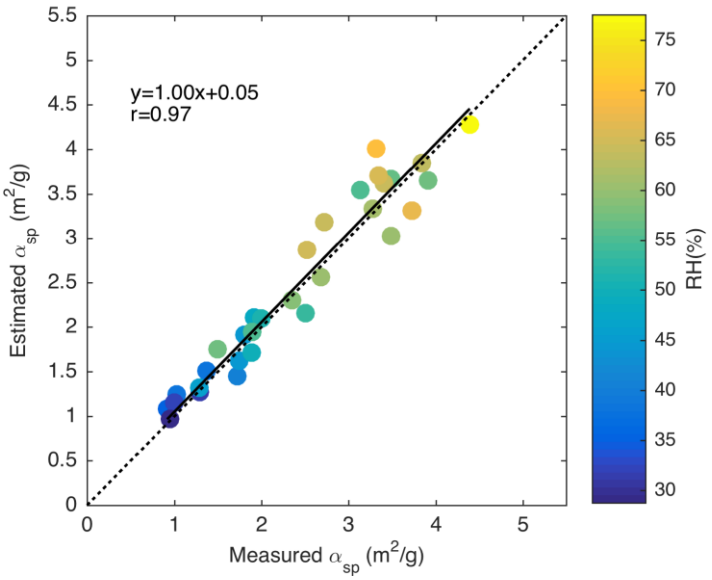

Figure 12. Average measured versus estimated α_{sp} at IMPROVE sites using revised optical tables for SIA and OA with geometric mean radii of 0.058μm, κ_s of 0.58 and κ_o of 0.10. The 1:1 line is black. Slope, offset and correlation coefficient are inset.

Figure 13 shows measured vs estimated α_{sp} in conditions dominated by different aerosol types using the revised optical tables. The overestimation of α_{sp} in SIA dominant conditions seen in Figure 5 has been eliminated, with a slope of 1.00 and a decreased offset (0.79 to 0.1). The large overestimation of α_{sp} that was apparent in OA dominant conditions has been significantly reduced, with a decrease in the offset from 0.87 to 0.44. α_{sp} remains accurately estimated at the majority of dust dominant sites, with the outlier at the site in Washington still skewing the best fit line. The slight overestimation of α_{sp} that was present in the PM_{coarse} dominant case using default optical tables has been eliminated using the revised tables (offset 0.36 to 0.03). Moderate increases in correlation coefficients are apparent in all cases except for the SIA dominant case, where it decreased by 0.02.

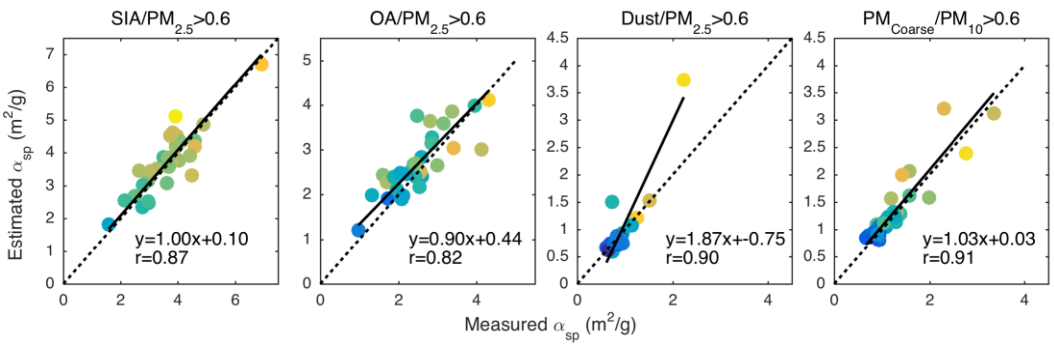

Figure **13**. Average measured versus estimated α_{sp} at IMPROVE sites using revised optical tables for SIA and OA. Results are shown for measurements taken in SIA dominant conditions, OA dominated conditions, dust dominant conditions and PM_{coarse} dominated conditions. The 1:1 line is black. Slope, offset and correlation coefficient are inset.

Figure 14 shows measured vs estimated α_{sp} using revised optical tables, divided into RH groups as in Figure 4. The overestimation in α_{sp} has been significantly reduced in the low RH case (slope=1.87 to slope=1.13) and in the mid RH case (slope=1.38 to slope=0.98). The slight overestimation in high RH conditions seen in Figure 4 has also been reduced, as shown by the decreased offset (0.84 to 0.65).

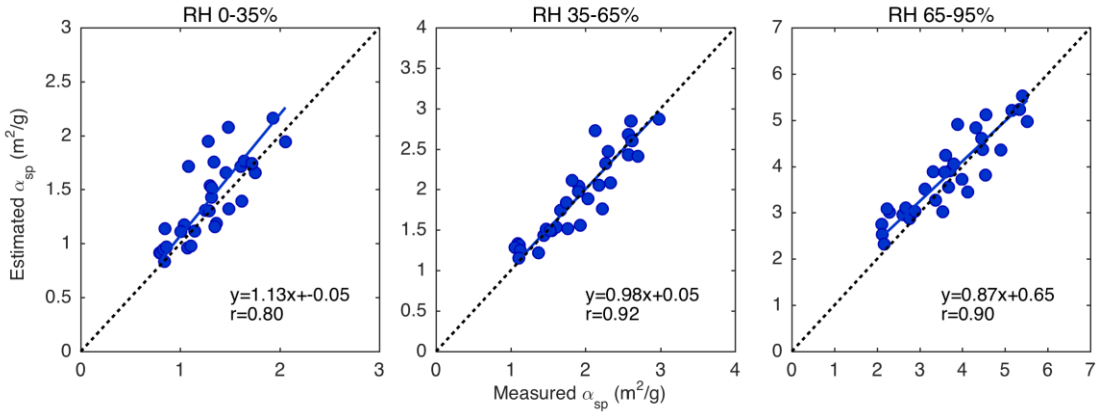

Figure 14. Average measured versus estimated α_{sp} at IMPROVE sites using revised optical tables for measurements taken in 0-35% RH, 35-65% RH and 65-95% RH conditions. The 1:1 line is black. Slope, offset and correlation coefficient are inset.

4.3 Changes in GEOS-Chem Simulated α_{sp}

Here, we examine how these changes to aerosol properties impact both GEOS-Chem simulation of mass scattering efficiency over North America and the fit between modeled and measured α_{sp} at IMPROVE sites. These simulations rely on GEOS-Chem simulations of aerosol composition using GEOS RH fields.

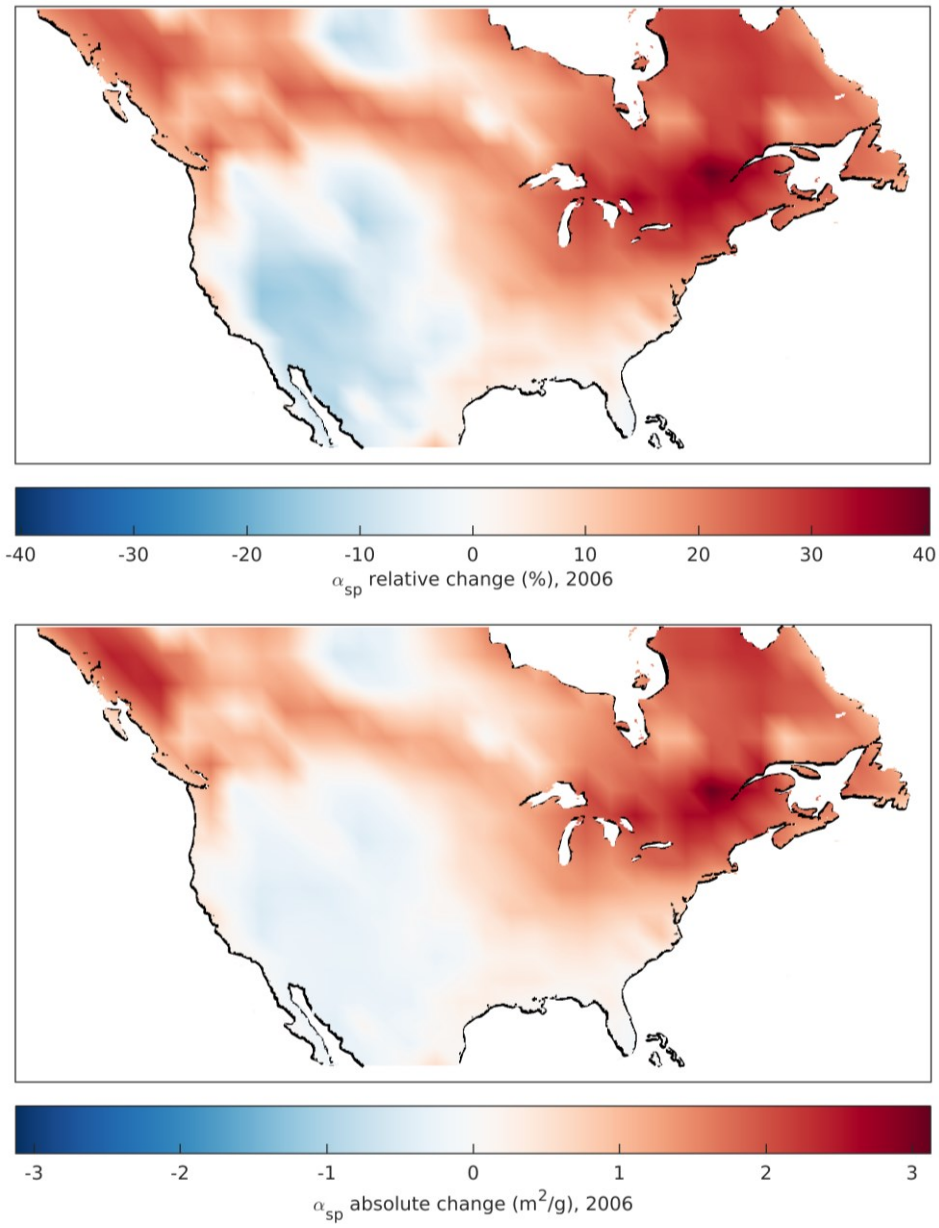

Figure 15. Average relative (top) and absolute (bottom) change in GEOS-Chem mass scattering efficiency over North America for the year 2006 after implementing revised optical tables for SIA and OA.

Figure 15 shows the relative and absolute change in mass scattering efficiency when switching from the default to revised optical tables. Continental mean α_{sp} increased by 12%. Increases in α_{sp} range from 20-40% in northeastern regions of North America, corresponding increases of 1-3 m^2/g. These larger changes reflect the higher RH and SIA fractions. Decreases in α_{sp} of up to 15% or -0.5 m^2/g are found in the southwest where RH is low and mineral dust dominates.

Figure 16 shows GEOS-Chem annual average mass scattering efficiency using default (top) and revised (bottom) optical tables over North America for the year 2006. The overlaying circles represent average measured α_{sp} at IMPROVE network sites for the year 2006, and the outer rings show the coincident simulated α_{sp} for each site. We exclude sites within 1° of the coast, as well as sites where elevation differs from average gridbox elevation by more than 1500 meters. These criteria result in a decrease from 24 to 19 in the number of sites available for the analysis in 2006.

Using default optical tables, simulated continental mean α_{sp} is 5.4 m^2/g. A maximum α_{sp} of 10 m^2/g occurs in the northwest, and a minimum α_{sp} of 1.7 m^2/g occurs in the southwest. Using revised optical tables, simulated continental mean α_{sp} is 6.2 m^2/g, with a maximum of 12.2 m^2/g in the northwest, and a minimum of 1.5 m^2/g in the southwest.

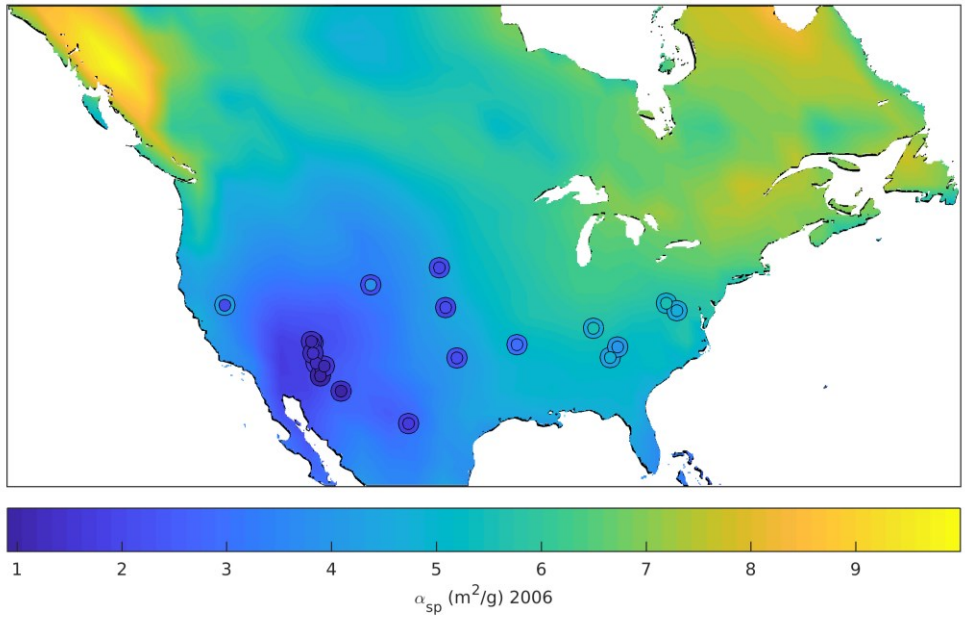

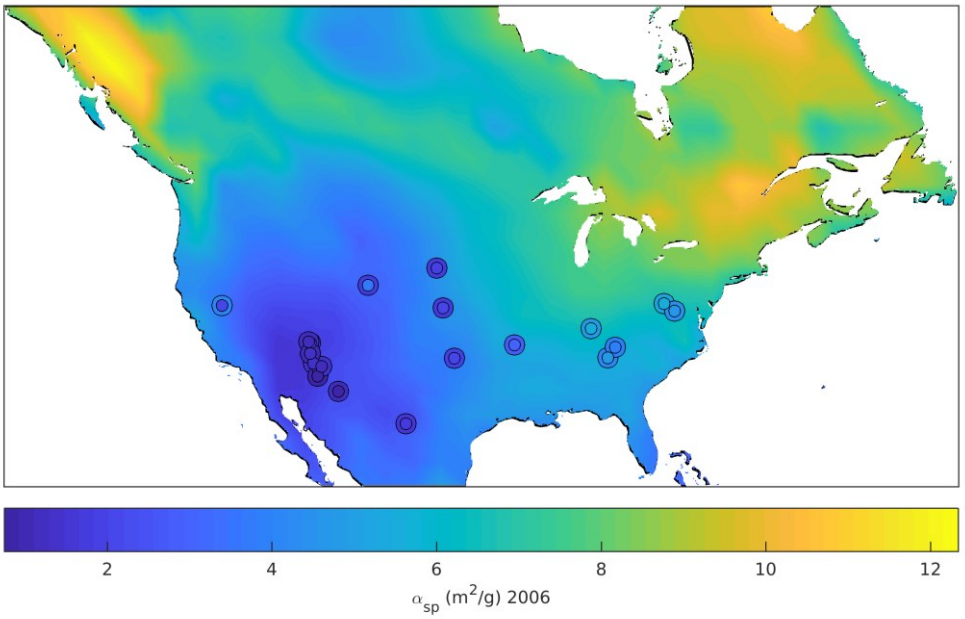

Figure 16. GEOS-Chem annual average mass scattering efficiency for the year 2006 using default (top) and revised (bottom) size and hygroscopicity for SIA and OA. Overlaying inner circles represent annual averages of α_{sp} at IMPROVE network sites for the year 2006. Outer rings represent coincident average simulated α_{sp}.

Figure 17 (left) shows coincident measured vs simulated mass scattering efficiency at the 19 IMPROVE sites, using default optical tables. Correlation is significant (r=0.88), but a bias in simulated α_{sp} is apparent (slope=0.83). Simulated α_{sp} is biased low at 3 sites in the

southeastern United States where average α_{sp} is largest, and simulated α_{sp} is biased high at 5 sites in the southwestern United States where average mass scattering efficiency is lowest.

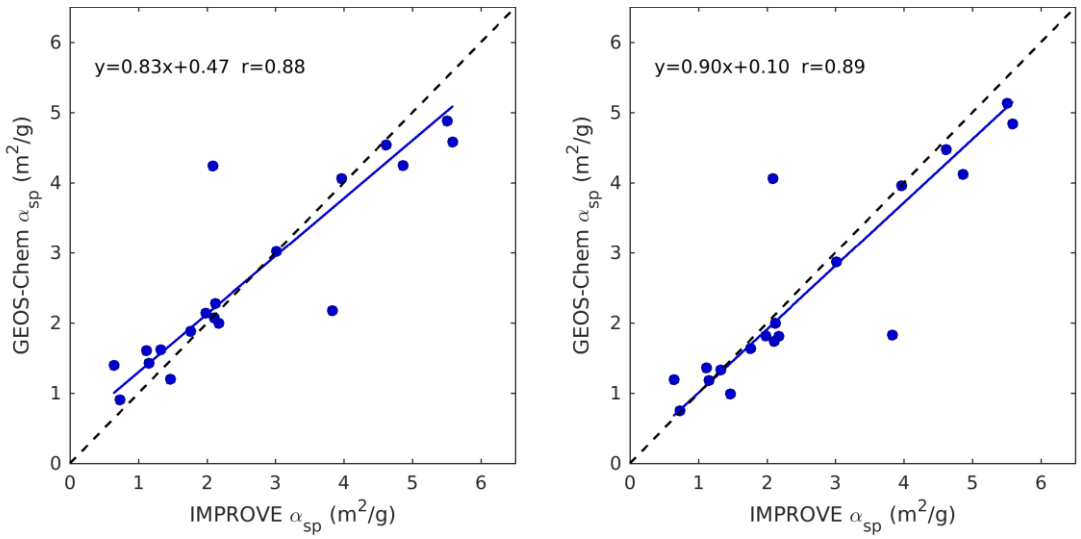

Figure 17. Coincident simulated versus measured average mass scattering efficiency (m^2/g) for the year 2006, using default (left) and revised (right) optical tables. Slope, offset and correlation coefficient are inset.

Sites with lowest average RH correspond to those with the lowest average mass scattering efficiency and vice versa. The tendency of mass scattering efficiency to be overestimated at low RH reflects the tendency that was originally seen in Figure 4.

Figure 17 (right) shows coincident measured vs simulated α_{sp} using revised optical tables. Correlation remains significant (r=0.89), and a decrease in bias is evident from the increase in slope (0.83 to 0.90) and decrease in offset (0.47 to 0.10). Most sites now lie closer to the 1:1 line. The overestimation of simulated α_{sp} in the southwest where RH is low has been reduced or eliminated at all sites.

4.4 Comparison with AERONET Measurements

Appendix B investigates changes to simulated AOD, and compares measured and simulated AOD at AERONET sites. Continental mean AOD increases by 29% over North America using revised optical tables (Figure B.2). Despite this overall increase in simulated AOD, the underestimation of simulated AOD across North America worsens in comparison to AERONET measurements after implementing the revised optical tables (Figure B.5). Globally, we see an average increase in AOD of 18% using revised optical tables, and comparison between simulated and measured AOD improves (Figures B.7 and B.9).

Chapter 5. Conclusions

The current representation of mass scattering efficiency in the GEOS-Chem global chemical transport model was evaluated using collocated ground-based measurements of particle mass, speciation, scatter and relative humidity from the IMPROVE network.

Calculated mass scattering efficiency had a positive bias using default physical and optical properties used in the GEOS-Chem model. This bias was most significant when $PM_{2.5}$ mass was dominated by secondary inorganic aerosols (SIA) or organic aerosols (OA). $PM_{2.5}$ dust and coarse particulate matter were accurately represented at the majority of IMPROVE sites.

Relative humidity played an important role in the severity of the bias in mass scattering efficiency. α_{sp} was overestimated by 87% in dry conditions (RH<35%). This bias was largest in the winter (87%) and smallest in the summer (29%). Implementing an efflorescence relative humidity for SIA and thus inhibiting hygroscopic growth below 35% RH decreased the dry bias by 34%. An annual representative dry geometric mean radius of 0.058 μm for SIA and OA decreased the dry mass scattering efficiency of these aerosols, and subsequently further reduced the bias in dry conditions to 13%.

κ-Kohler theory was implemented for the hygroscopic growth of SIA and OA, which is characterized by smaller growth factors at low RH and larger growth factors at high RH compared to default growth factors in GEOS-Chem. κ values of 0.58 for SIA and 0.10 for OA eliminated the overall bias in estimated mass scattering efficiency.

These changes to SIA and OA optical tables resulted in a continental mean increase in GEOS-Chem simulated mass scattering efficiency of 12%. Northeastern regions of North America saw the largest increases (20-40%) due to high RH and SIA fractions, while southwestern regions of the continent saw decreases in α_{sp} of up to 15% due to low RH and high dust fractions. These changes to the GEOS-Chem optical tables improved the fit between measured and simulated mass scattering efficiency at IMPROVE sites, reflected in the changes to the slope (0.83 to 0.90) and the offset (0.47 to 0.10).

Future work should expand analysis of the representation of mass scattering efficiency, by incorporating measurements from other ground based measurement networks such as the Surface PARTiculate MAtter network (SPARTAN), which provides measurements of particulate mass, speciation and scatter in populated regions worldwide (Snider et al., 2015; Snider et al., 2016). Such comparisons may also be useful to evaluate and improve prognostic simulations of aerosol size (Adams & Seinfeld, 2002).

References

Adams, P. J., & Seinfeld, J. H. (2002). Predicting global aerosol size distributions in general circulation models, *107*, 1–23. https://doi.org/10.1029/2001JD001010

Bey, I., Jacob, D. J., Yantosca, R. M., Logan, J. A., Field, B. D., Fiore, A. M., … Schultz, M. G. (2001). Global Modeling of Tropospheric Chemistry with Assimilated Meteorology: Model Description and Evaluation. *Journal of Geophysical Research*, *106*, 73–95. https://doi.org/10.1029/2001JD000807

Ciobanu, V. G., Marcolli, C., Krieger, U. K., Zuend, A., & Peter, T. (2010). Efflorescence of ammonium sulfate and coated ammonium sulfate particles: Evidence for surface nucleation. *Journal of Physical Chemistry A*, *114*(35), 9486–9495. https://doi.org/10.1021/jp103541w

Dougle, P. G., Veefkind, J. P., & R, H. M. B. (1998). Crystallisation of mixtures of ammonium nitrate, ammonium sulphate and soot, *29*(3), 375–386.

Drury, E., Jacob, D. J., Spurr, R. J. D., Wang, J., Shinozuka, Y., Anderson, B. E., … Weber, R. (2010). Synthesis of satellite (MODIS), aircraft (ICARTT), and surface (IMPROVE, EPA-AQS, AERONET) aerosol observations over eastern North America to improve MODIS aerosol retrievals and constrain surface aerosol concentrations and sources. *Journal of Geophysical Research Atmospheres*, *115*(14), 1–17. https://doi.org/10.1029/2009JD012629

Duplissy, J., De Carlo, P. F., Dommen, J., Alfarra, M. R., Metzger, A., Barmpadimos, I., … Baltensperger, U. (2011). Relating hygroscopicity and composition of organic aerosol particulate matter. *Atmospheric Chemistry and Physics*, *11*(3), 1155–1165. https://doi.org/10.5194/acp-11-1155-2011

Dusek, U., Frank, G. P., Massling, A., Zeromskiene, K., Iinuma, Y., Schmid, O., … Andreae, M. O. (2011). Water uptake by biomass burning aerosol at sub-and supersaturated conditions: Closure studies and implications for the role of organics. *Atmospheric Chemistry and Physics*, *11*(18), 9519–9532. https://doi.org/10.5194/acp-11-9519-2011

Fairlie, D. T., Jacob, D. J., & Park, R. J. (2007). The impact of transpacific transport of mineral dust in the United States. *Atmospheric Environment*, *41*(6), 1251–1266. https://doi.org/10.1016/j.atmosenv.2006.09.048

Fairlie, T. D., Jacob, D. J., Dibb, J. E., Alexander, B., Avery, M. A., Van Donkelaar, A., & Zhang, L. (2010). Impact of mineral dust on nitrate, sulfate, and ozone in transpacific Asian pollution plumes. *Atmospheric Chemistry and Physics*, *10*(8), 3999–4012. https://doi.org/10.5194/acp-10-3999-2010

Fehsenfeld, F. C., Ancellet, G., Bates, T. S., Goldstein, A. H., Hardesty, R. M., Honrath, R., … Zbinden, R. (2006). International Consortium for Atmospheric Research on Transport and Transformation (ICARTT): North America to Europe - Overview of the 2004 summer field study. *Journal of Geophysical Research Atmospheres*, *111*(23). https://doi.org/10.1029/2006JD007829

Fountoukis, C., & Nenes, A. (2007). ISORROPIA II: a computationally efficient thermodynamic equilibrium model for K –H 2 O aerosols. *Atmos. Chem. Phys. Atmospheric Chemistry and Physics*, *7*, 4639–4659. https://doi.org/10.5194/acp-7-4639-2007

Hand, J. L., & Malm, W. C. (2007). Review of aerosol mass scattering efficiencies from ground-based measurements since 1990. *Journal of Geophysical Research Atmospheres*, *112*(16). https://doi.org/10.1029/2007JD008484

Hersey, S. P., Craven, J. S., Metcalf, A. R., Lin, J., Lathem, T., Suski, K. J., … Seinfeld, J. H. (2013). Composition and hygroscopicity of the Los Angeles Aerosol: CalNex. *Journal of Geophysical Research Atmospheres*, *118*(7), 3016–3036. https://doi.org/10.1002/jgrd.50307

Holben, B. N., Eck, T. F., Slutsker, I., Tanré, D., Buis, J. P., Setzer, A., … Smirnov, A. (1998). AERONET—A Federated Instrument Network and Data Archive for Aerosol Characterization. *Remote Sensing of Environment*, *66*(1), 1–16. https://doi.org/10.1016/S0034-4257(98)00031-5

Jaeglé, L., Quinn, P. K., Bates, T. S., Alexander, B., & Lin, J. T. (2011). Global distribution of sea salt aerosols: New constraints from in situ and remote sensing observations. *Atmospheric Chemistry and Physics*, *11*(7), 3137–3157. https://doi.org/10.5194/acp-11-3137-2011

Jimenez, J. L., Canagaratna, M. R., Donahue, N. M., Prevot, a. S. H., Zhang, Q., Kroll, J. H., … Worsnop, D. R. (2009). Evolution of Organic Aerosols in the Atmosphere. *Science*, *326*(5959), 1525–1529. https://doi.org/10.1126/science.1180353

Kahn, R. A., Gaitley, B. J., Martonchik, J. V., Diner, D. J., Crean, K. A., & Holben, B. (2005). Multiangle Imaging Spectroradiometer (MISR) global aerosol optical depth validation based on 2 years of coincident Aerosol Robotic Network (AERONET) observations. *Journal of Geophysical Research D: Atmospheres*, *110*(10), 1–16. https://doi.org/10.1029/2004JD004706

Koepke, P., Hess, M., Schult, I., & Shettle, E. P. (1997). *Global Aerosol Data Set*. *Max-Planck-Institut fur Meteorologie*. https://doi.org/ISSN: 0937-1060

Kreidenweis, S. M., Petters, M. D., & DeMott, P. J. (2008). Single-parameter estimates of aerosol water content. *Environmental Research Letters*, *3*(3), 35002. https://doi.org/10.1088/1748-9326/3/3/035002

Lowenthal, D., & Kumar, N. (2006). Light scattering from sea-salt aerosols at interagency monitoring of protected visual environments (IMPROVE) sites. *Journal of the Air & Waste Management*, *56*(5), 636–642. https://doi.org/10.1080/10473289.2006.10464478

Malm, C., Sisler, J. F., & Cahill, A. (1994). Spatial and seasonal trends in particle concentration and optical extinction in the United States, *99*, 1347–1370.

Malm, W. C. (2004). Spatial and monthly trends in speciated fine particle concentration in the United States. *Journal of Geophysical Research*, *109*(D3), D03306. https://doi.org/10.1029/2003JD003739

Malm, W. C., & Hand, J. L. (2007). An examination of the physical and optical properties of aerosols collected in the IMPROVE program. *Atmospheric Environment*, *41*(16), 3407–3427. https://doi.org/10.1016/j.atmosenv.2006.12.012

Malm, W. C., Pitchford, M. L., McDade, C., & Ashbaugh, L. L. (2007). Coarse particle speciation at selected locations in the rural continental United States. *Atmospheric Environment*, *41*(10), 2225–2239. https://doi.org/10.1016/j.atmosenv.2006.10.077

Martin, S. T., Rosenoern, T., Chen, Q., & Collins, D. R. (2008). Phase changes of ambient particles in the Southern Great Plains of Oklahoma. *Geophysical Research Letters*, *35*(22), 1–5. https://doi.org/10.1029/2008GL035650

Martin, S. T., Schlenker, J. C., Malinowski, A., & Hung, H. (2003). Crystallization of atmospheric sulfate-nitrate-ammonium particles, *30*(21), 1–4. https://doi.org/10.1029/2003GL017930

Martin, R. V. (2003). Global and regional decreases in tropospheric oxidants from photochemical effects of aerosols. *Journal of Geophysical Research*, *108*(D3), 4097. https://doi.org/10.1029/2002JD002622

Mishchenko, M. I., Dlugach, J. M., Yanovitskij, E. G., & Zakharova, N. T. (1999). Bidirectional reflectance of flat, optically thick particulate layers: An efficient radiative transfer solution and applications to snow and soil surfaces. *Journal of Quantitative Spectroscopy and Radiative Transfer*, *63*(2–6), 409–432. https://doi.org/10.1016/S0022-4073(99)00028-X

Ng, N. L., Canagaratna, M. R., Zhang, Q., Jimenez, J. L., Tian, J., Ulbrich, I. M., … Worsnop, D. R. (2010). Organic aerosol components observed in Northern Hemispheric datasets from Aerosol Mass Spectrometry. *Atmospheric Chemistry and Physics*, *10*(10), 4625–4641. https://doi.org/10.5194/acp-10-4625-2010

Park, R. J. (2003). Sources of carbonaceous aerosols over the United States and implications for natural visibility. *Journal of Geophysical Research*, *108*(D12),

4355. https://doi.org/10.1029/2002JD003190

Park, R. J., Jacob, D. J., Field, B. D., Yantosca, R. M., & Chin, M. (2004). Natural and transboundary pollution influences on sulfate-nitrate-ammonium aerosols in the United States: Implications for policy. *Journal of Geophysical Research D: Atmospheres*, *109*(15). https://doi.org/10.1029/2003JD00473

Petters, M. D., & Kreidenweis, S. M. (2007). A single parameter representation of hygroscopic growth and cloud\ncondensation nucleus activity. *Atmos. Chem. Phys.*, 1961–1971. https://doi.org/10.5194/acp-7-1961-2007

Petters, M. D., & Kreidenweis, S. M. (2013). A single parameter representation of hygroscopic growth and cloud condensation nucleus activity-Part 3: Including surfactant partitioning. *Atmospheric Chemistry and Physics*, *13*(2), 1081–1091. https://doi.org/10.5194/acp-13-1081-2013

Philip, S., Martin, R. V., Pierce, J. R., Jimenez, J. L., Zhang, Q., Canagaratna, M. R., … Krotkov, N. A. (2014). Spatially and seasonally resolved estimate of the ratio of organic mass to organic carbon. *Atmospheric Environment*, *87*, 34–40. https://doi.org/10.1016/j.atmosenv.2013.11.065

Pye, H. O. T., Chan, A. W. H., Barkley, M. P., & Seinfeld, J. H. (2010). Global modeling of organic aerosol: The importance of reactive nitrogen (NOx and NO3). *Atmospheric Chemistry and Physics*, *10*(22), 11261–11276. https://doi.org/10.5194/acp-10-11261-2010

Pye, H. O. T., Liao, H., Wu, S., Mickley, L. J., Jacob, D. J., Henze, D. J., & Seinfeld, J. H. (2009). Effect of changes in climate and emissions on future sulfate-nitrate-ammonium aerosol levels in the United States. *Journal of Geophysical Research Atmospheres*, *114*(1), 1–18. https://doi.org/10.1029/2008JD010701

Rickards, A. M. J., Miles, R. E. H., Davies, J. F., Marshall, F. H., & Reid, J. P. (2013). Measurements of the sensitivity of aerosol hygroscopicity and the κ parameter to the O/C ratio. *Journal of Physical Chemistry A*, *117*(51), 14120–14131. https://doi.org/10.1021/jp407991n

Ridley, D. A., Heald, C. L., & Ford, B. (2012). North African dust export and deposition: A satellite and model perspective. *Journal of Geophysical Research Atmospheres*, *117*(2), 1–21. https://doi.org/10.1029/2011JD016794

Singh, H. B., Brune, W. H., Crawford, J. H., Jacob, D. J., & Russell, P. B. (2006). Overview of the summer 2004 Intercontinental Chemical Transport Experiment-North America (INTEX-A). *Journal of Geophysical Research Atmospheres*, *111*(24). https://doi.org/10.1029/2006JD007905

Snider, G., Weagle, C. L., Martin, R. V., Van Donkelaar, A., Conrad, K., Cunningham,

D., … Liu, Y. (2015). SPARTAN: A global network to evaluate and enhance satellite-based estimates of ground-level particulate matter for global health applications. *Atmospheric Measurement Techniques*, *8*(1), 505–521. https://doi.org/10.5194/amt-8-505-2015

Snider, G., Weagle, C. L., Murdymootoo, K. K., Ring, A., Ritchie, Y., Stone, E., … Martin, R. V. (2016). Variation in global chemical composition of PM2.5: emerging results from SPARTAN. *Atmospheric Chemistry and Physics*, *16*(15), 9629–9653. https://doi.org/10.5194/acp-16-9629-2016

Solomon, P. A., Crumpler, D., Flanagan, J. B., Jayanty, R. K. M., Rickman, E. E., & McDade, C. E. (2014). U.S. National PM2.5 Chemical Speciation Monitoring Networks-CSN and IMPROVE: Description of Networks. *Journal of the Air & Waste Management Association*, *64*(12), 1410–38. https://doi.org/10.1080/10962247.2014.956904

Stanier, C. O., Khlystov, A. Y., & Pandis, S. N. (2004). Ambient aerosol size distributions and number concentrations measured during the Pittsburgh Air Quality Study (PAQS). *Atmospheric Environment*, *38*(20), 3275–3284. https://doi.org/10.1016/j.atmosenv.2004.03.020

van Donkelaar, A., Martin, R. V., Brauer, M., Kahn, R., Levy, R., Verduzco, C., & Villeneuve, P. J. (2010). Global estimates of ambient fine particulate matter concentrations from satellite-based aerosol optical depth: Development and application. *Environmental Health Perspectives*, *118*(6), 847–855. https://doi.org/10.1289/ehp.0901623

Wang, Q., Jacob, D. J., Spackman, J. R., Perring, A. E., Schwarz, J. P., Moteki, N., … Barrett, S. R. H. (2014). Global budget and radiative forcing of black carbon aerosol : Constraints from pole-to-pole (HIPPO) observations across the Paci fi c, *119*, 195–206. https://doi.org/10.1002/2013JD020824

White, W. H., Macias, E. S., Nininger, R. C., & Schorran, D. (1994). Size-resolved measurements of light scattering by ambient particles in the southwestern U.S.A. *Atmospheric Environment*, *28*(5), 909–921. https://doi.org/10.1016/1352-2310(94)90249-6

Zhang, L., Kok, J. F., Henze, D. K., Li, Q., & Zhao, C. (2013). Improving simulations of fine dust surface concentrations over the western United States by optimizing the particle size distribution. *Geophysical Research Letters*, *40*(12), 3270–3275. https://doi.org/10.1002/grl.50591

Appendix A: Default and Revised Optical Tables for SIA and OA

Aerosol	RH	Default				Revised		(κ_s=0.58	κ_o=0.10)
		r_g (μm)	r_{eff} (μm)	Q	SSA	r_g (μm)	r_{eff} (μm)	Q	SSA
SIA	0	0.069	0.121	0.902	0.965	0.058	0.101	0.603	0.959
	35	0.081	0.141	0.965	0.975	0.065	0.112	0.638	0.968
	50	0.086	0.149	0.992	0.979	0.068	0.117	0.653	0.972
	70	0.093	0.163	1.062	0.983	0.077	0.134	0.734	0.980
	80	0.100	0.174	1.137	0.986	0.087	0.150	0.835	0.986
	90	0.114	0.198	1.301	0.991	0.107	0.185	1.095	0.993
	95	0.131	0.227	1.517	0.994	0.133	0.231	1.470	0.996
	99	0.175	0.304	1.272	0.993	0.225	0.391	2.541	0.999
OA	0	0.073	0.127	1.007	0.966	0.058	0.101	0.603	0.959
	35	0.078	0.135	0.965	0.972	0.059	0.103	0.608	0.965
	50	0.080	0.139	0.947	0.975	0.060	0.104	0.610	0.963
	70	0.083	0.145	0.947	0.978	0.063	0.108	0.622	0.966
	80	0.086	0.149	0.955	0.980	0.065	0.113	0.639	0.970
	90	0.092	0.159	0.990	0.984	0.073	0.125	0.696	0.977
	95	0.099	0.171	1.053	0.988	0.084	0.144	0.811	0.985
	99	0.117	0.203	1.273	0.993	0.132	0.223	1.463	0.996

Table A. 1 Default and revised aerosol size and optical properties for SIA and OA at 8 relative humidity values. κ_o=0.10, κ_s=0.58.

Appendix B: Impacts to GC Simulated AOD; North America and Global Comparison with AERONET Measurements

B.1 AERONET Measurements: North America

The *Ae*rosol *Ro*botics *Net*work (AERONET) is a long-term network of ground based sun photometers that provides continuous, cloud-screened measurements of aerosol optical depth (AOD) at several fixed wavelengths in the visible and near infrared (Holben et al., 1998). The calculation of AOD in GEOS-Chem is performed using simulated mass concentrations of aerosol species and mass extinction efficiencies, summed over all vertical layers. Our analysis of mass scattering efficiency can therefore be extended globally by comparing GEOS-Chem calculated AOD to AOD measured at AERONET sites. During our simulation year of 2006, AERONET consisted of 231 sites across the globe with 26 sites located in the Canada and the United States. Figure B.1 shows AERONET sites in North America; the overlaying circles represent the average AOD at each site for the year 2006.

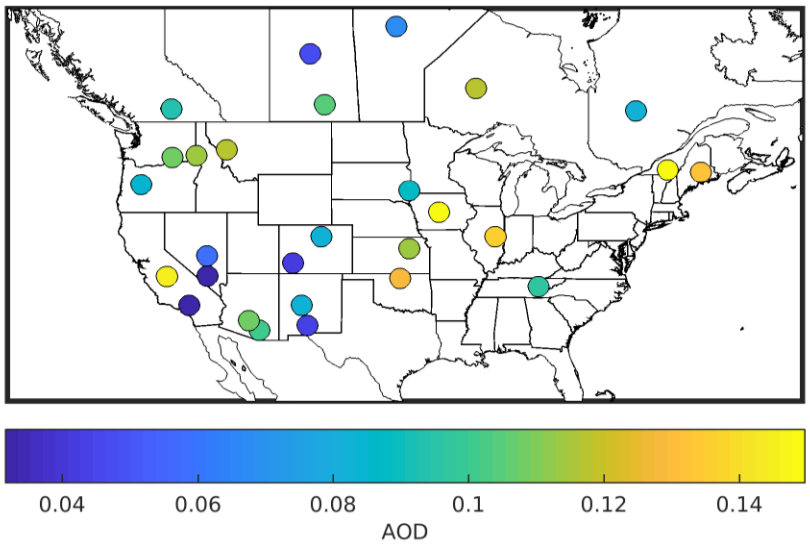

Figure B. 1 Map of AERONET sites across North America in 2006. Overlaying circles represent average AOD at each site during this year.

B.2 Changes in GEOS-Chem Simulated AOD: North America

Here we examine how the changes to SIA and OA properties impact GEOS-Chem simulation of aerosol optical depth over North America.

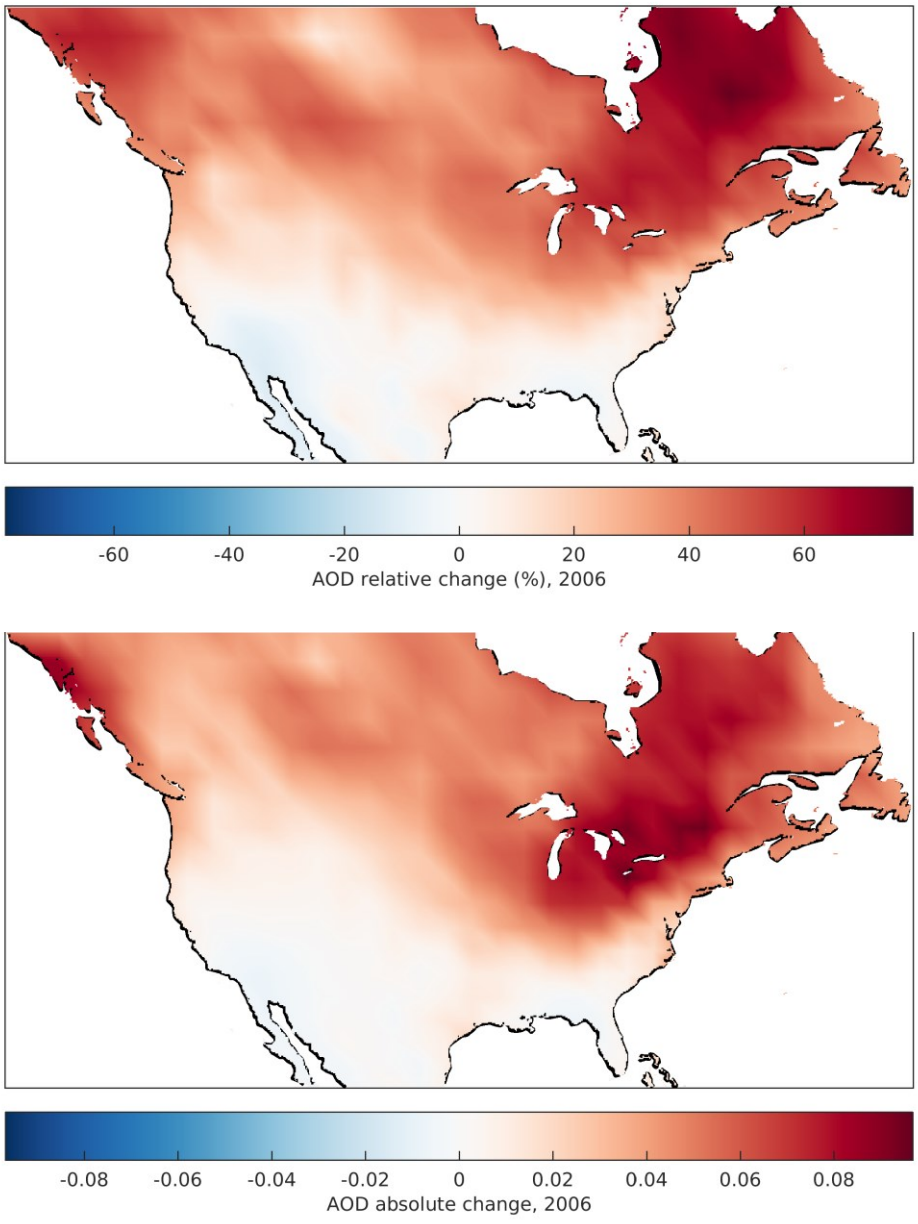

Figure B. 2 Average relative (top) and absolute (bottom) change in GEOS-Chem aerosol optical depth over North America for the year 2006 after implementing revised optical tables for SIA and OA.

Figure B.2 shows the relative and absolute change in AOD when switching from the default to revised optical tables. Continental mean AOD increased by 29%. Increases in AOD range from 60-80% in northeastern regions of North America, corresponding to an increase in AOD of 0.08-0.1. Northeastern U.S. sees the largest absolute increases in AOD, due to the high average RH and SIA fractions. Decreases in AOD between 0-12% are present in southern parts of the continent, where average RH is low, as shown in Figure B.3.

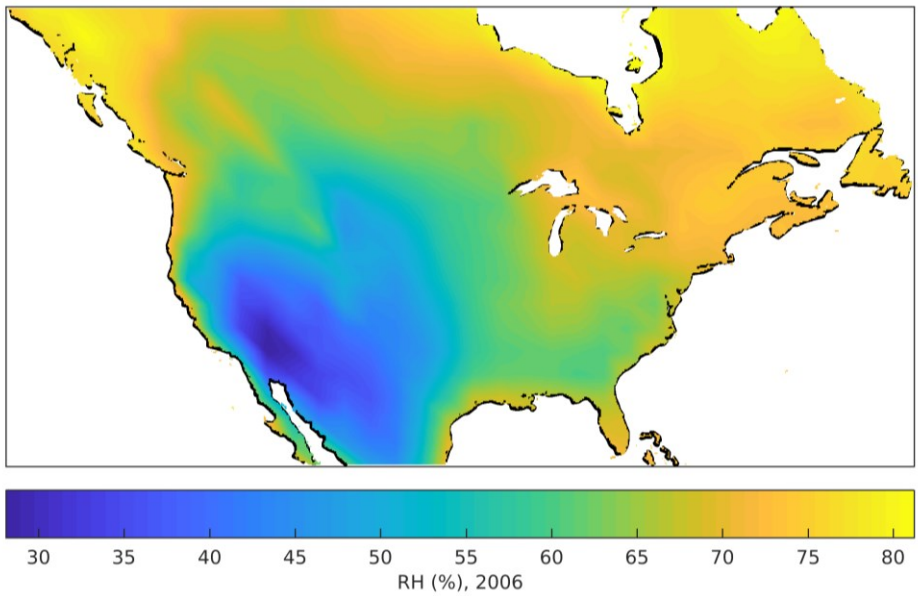

Figure B. 3 Average GEOS-Chem simulated relative humidity over North America for 2006.

B.3 Comparison of Measured and Simulated AOD: North America

Figure B.4 shows GEOS-Chem annual average AOD using default (top) and revised (bottom) optical tables over North America for the year 2006. The overlaying circles represent average measured AOD at AERONET sites for the year 2006, and the outer rings show the coincident simulated AOD for each site. We exclude sites within 1° of the coast, as well as sites where elevation differs from average gridbox elevation by more

than 1500 meters. We also exclude sites where average $PM_{2.5}$ is dominated by dust ($dust/PM_{2.5}>0.6$), to focus on the representation of the optical properties of SIA and OA. Using the default optical tables, continental mean AOD is 0.13. AOD is largest in the northeastern U.S. and in one area in the north. Minimums in AOD occur in the southwest of the continent. Using the revised optical tables, continental mean AOD is 0.17, and spatial trends are unchanged.

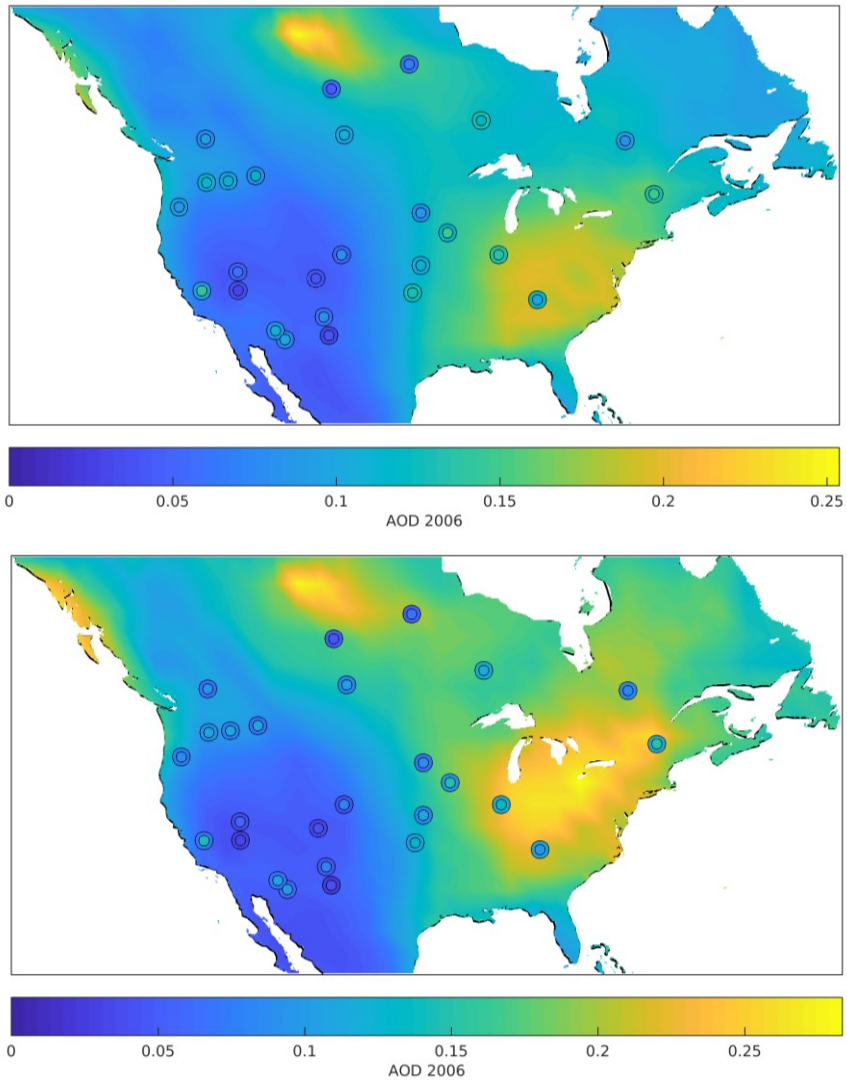

Figure B. 4 GEOS-Chem annual aerosol optical depth for the year 2006 using default (top) and revised (bottom) size and hygroscopicity for SIA and OA. Overlaying inner circles represent annual averages of AOD at AERONET sites for the year 2006. Outer rings represent coincident average simulated AOD.

Figure B.5 shows coincident measured vs simulated AOD at AERONET sites for default (left) and revised (right) optical tables. AOD is underestimated at the majority of sites in North America using the default tables. Coincident simulated AOD decreases after implementing the revised optical tables, and so this underestimation of AOD is exacerbated over North America.

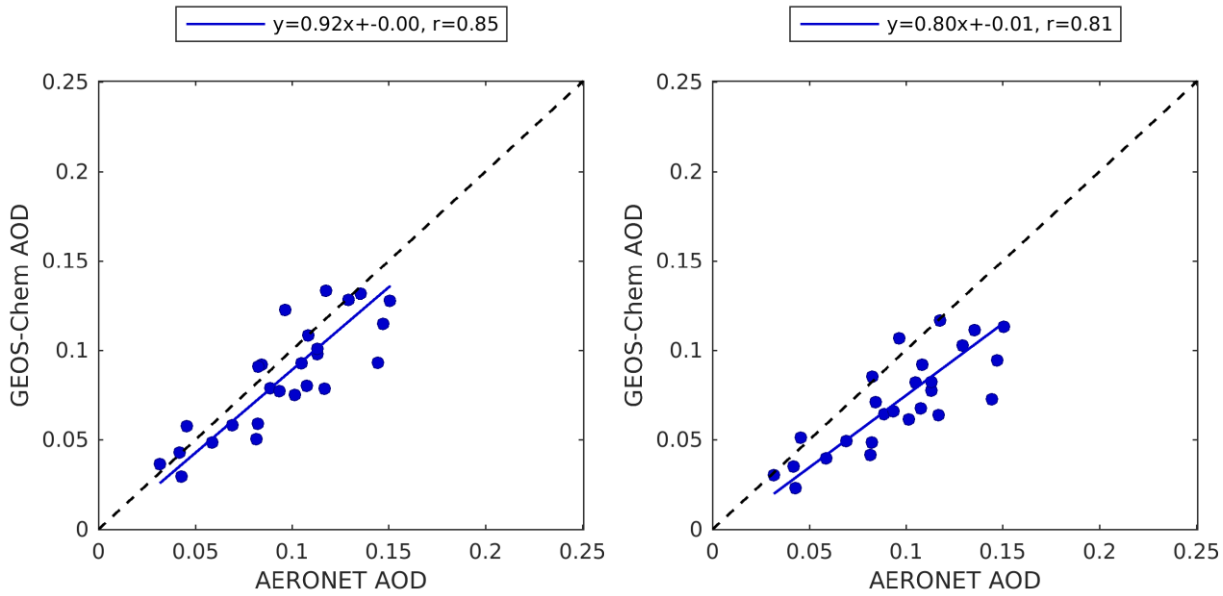

Figure B. 5 Coincident simulated versus measured AOD at AERONET sites for the year 2006, using default (left) and revised (right) size and hygroscopicity. Slope, offset and correlation coefficient are inset. The 1:1 line is shown in black.

B.4 AERONET Measurements: Global

Figure B.6 shows global AERONET sites in 2006; the overlaying circles represent the average AOD at each site for the year 2006. Measured AOD is elevated over parts of southeast Asia and south of the Sahara Desert.

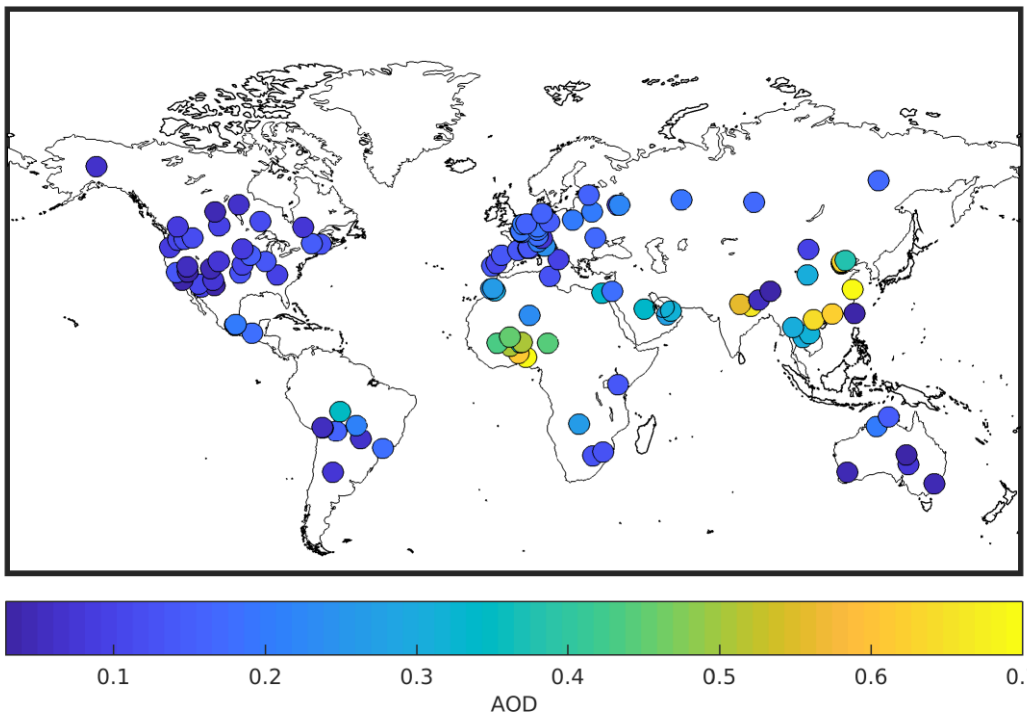

Figure B. 6 Map of all AERONET sites in 2006. Overlaying circles represent average AOD at each site during this year.

B.4 Changes in GEOS-Chem Simulated AOD: Global

Here we examine how the changes to SIA and OA properties impact GEOS-Chem simulated AOD globally.

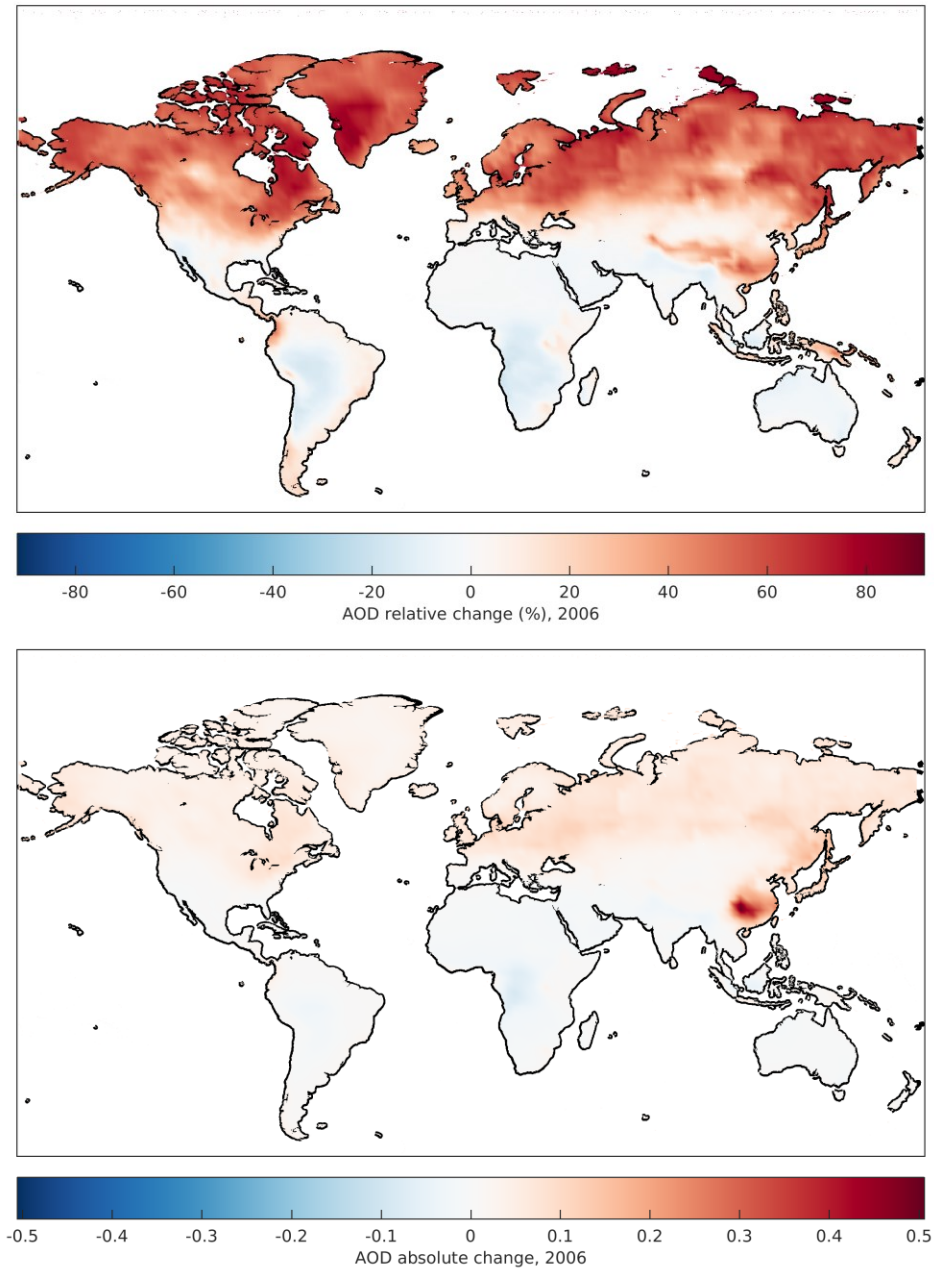

Figure B. 7 Average relative (top) and absolute (bottom) change in GEOS-Chem aerosol optical depth globally for the year 2006 after implementing revised optical tables for SIA and OA.

Figure B.7 shows the relative (top) and absolute (bottom) changes in AOD. Global mean AOD increases by 18%. Relative changes in AOD are most pronounced in Northern regions where mean relative humidity is high, with increases in simulated AOD ranging from 50-90 %. Decreases in AOD between 0-20% are present in most of the southern hemisphere, in part due to the lower average RH. Absolute changes in AOD show a similar trend, with slight increases in AOD of up to 0.2 in northern regions, and slight decreases of up of -0.09 in southern regions. An exception to this is seen over parts of China, where AOD increases by 0.5 due to the elevated SIA and OA concentrations.

B.5 Comparison of Measured and Simulated AOD: Global

Figure B.8 shows coincident measured (inner circles) and simulated (outer rings) AOD for the year 2006, using the same site filtering protocol as described in section B.3. Across the globe, we see that AOD is both over and underestimated. AOD is overestimated at most sites in Africa, with the most notable overestimation at the site in Nigeria. AOD is moderately overestimated at sites in Australia. Underestimation of AOD occurs at most sites in South America, as well as at sites in southern North America and southern Asia.

Figure B.9 shows coincident measured vs simulated AOD at AERONET sites for default (left) and revised (right) optical tables. There is no change in the correlation coefficient ($r=0.78$), and the slope decreases from 1.12 to 0.99 when switching to the revised optical tables.

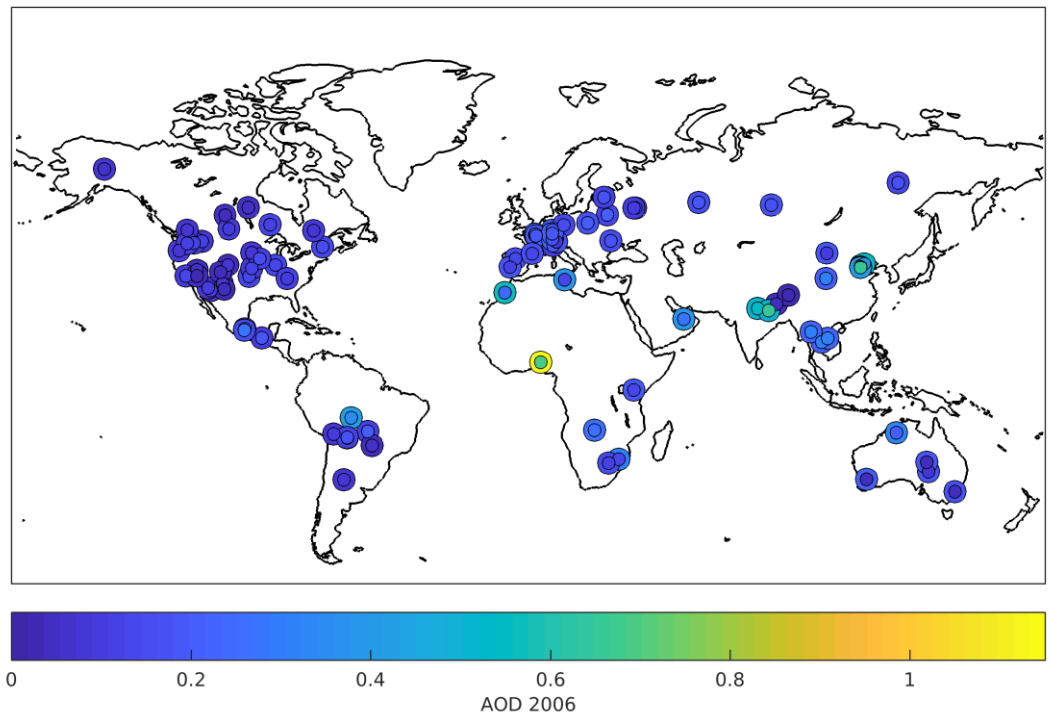

Figure B. 8 Global comparison of AERONET measured AOD (inner circles) and GEOS-Chem coincident simulated AOD (outer rings) for the year 2006 using default optical tables.

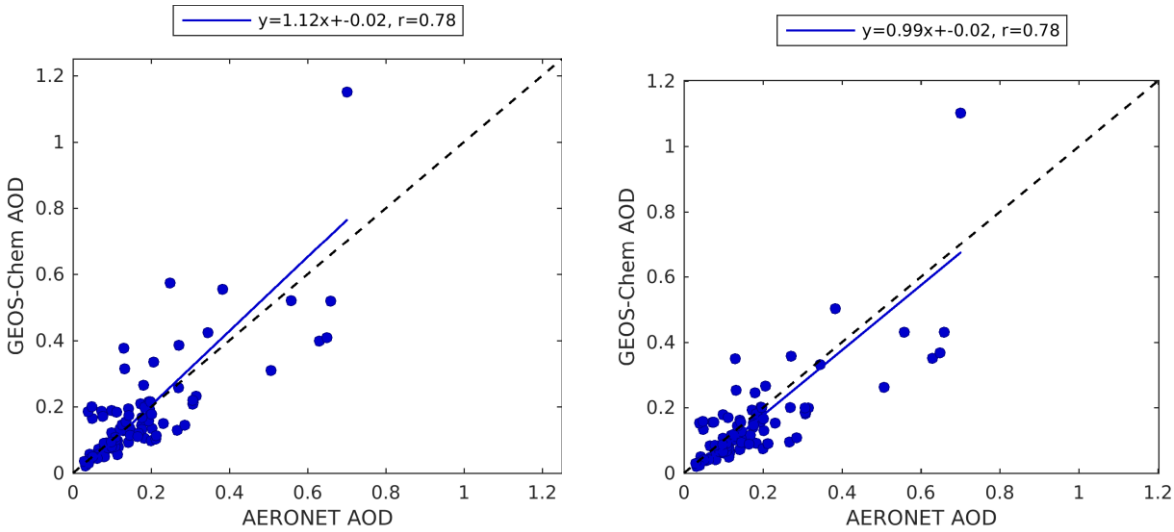

Figure B. 9 Coincident simulated versus measured AOD at AERONET sites for the year 2006, using default (left) and revised (right) sizes and hygroscopicity. Slope, offset and correlation coefficient are inset. The 1:1 line is shown in black.